A General Study of the Complex Ginzburg-Landau Equation

Weigang Liu

Dissertation submitted to the Faculty of the
Virginia Polytechnic Institute and State University
in partial fulfillment of the requirements for the degree of

Doctor of Philosophy
in
Physics

Uwe C. Täuber, Chair
Shengfeng Cheng
Vito W. Scarola
Eric R. Sharpe

May 3rd, 2019
Blacksburg, Virginia

Keywords: complex Ginzburg-Landau equation, critical dynamics, initial-slip exponent, aging scaling, nucleation phenomena

A General Study of the Complex Ginzburg-Landau Equation

Weigang Liu

(ABSTRACT)

In this dissertation, I study a nonlinear partial differential equation, the complex Ginzburg-Landau (CGL) equation. I first employed the perturbative field-theoretic renormalization group method to investigate the critical dynamics near the continuous non-equilibrium transition limit in this equation with additive noise. Due to the fact that time translation invariance is broken following a critical quench from a random initial configuration, an independent "initial-slip" exponent emerges to describe the crossover temporal window between microscopic time scales and the asymptotic long-time regime. My analytic work shows that to first order in a dimensional expansion with respect to the upper critical dimension, the extracted initial-slip exponent in the complex Ginzburg-Landau equation is identical to that of the equilibrium model A. Subsequently, I studied transient behavior in the CGL through numerical calculations. I developed my own code to numerically solve this partial differential equation on a two-dimensional square lattice with periodic boundary conditions, subject to random initial configurations. Aging phenomena are demonstrated in systems with either focusing and defocusing spiral waves, and the related aging exponents, as well as the autocorrelation exponents, are numerically determined. I also investigated nucleation processes when the system is transiting from a turbulent state to the "frozen" state. An extracted finite dimensionless barrier in the deep-quenched case and the exponentially decaying distribution of the nucleation times in the near-transition limit are both suggestive that the dynamical transition observed here is discontinuous. This research is supported by the U.

S. Department of Energy, Office of Basic Energy Sciences, Division of Materials Science and Engineering under Award DE-FG02-SC0002308

A General Study of the Complex Ginzburg-Landau Equation

Weigang Liu

(GENERAL AUDIENCE ABSTRACT)

The complex Ginzburg-Landau equation is one of the most studied nonlinear partial differential equation in the physics community. I study this equation using both analytical and numerical methods. First, I employed the field theory approach to extract the critical initial-slip exponent, which emerges due to the breaking of time translation symmetry and describes the intermediate temporal window between microscopic time scales and the asymptotic long-time regime. I also numerically solved this equation on a two-dimensional square lattice. I studied the scaling behavior in non-equilibrium relaxation processes in situations where defects are interactive but not subject to strong fluctuations. I observed nucleation processes when the system under goes a transition from a strongly fluctuating disordered state to the relatively stable "frozen" state where its dynamics cease. I extracted a finite dimensionless barrier for systems that are quenched deep into the frozen state regime. An exponentially decaying long tail in the nucleation time distribution is found, which suggests a discontinuous transition. This research is supported by the U. S. Department of Energy, Office of Basic Energy Sciences, Division of Materials Science and Engineering under Award DE-FG02-SC0002308

I dedicate this thesis to my beloved parents.

Acknowledgments

I am deeply grateful to my advisor, Prof. Uwe C. Täuber, for his tremendous help and support which extend from my research to my life. I benefited a lot from his philosophic feedback, sustained guidance during my Ph. D study, and especially his help in fixing my language problems. He kept encouraging me to practice my research skill and develop a more comprehensive understanding about physics. With his endorsement, I was also pursuing another related master degree in computer science, which also contributes to my study in physics the other way round. In a word, I am very proud of being in his group and working with him.

I would like to further express my gratitude to my PhD committee members: Prof. Eric Sharpe, Prof. Vito Scarola, and Prof. Shengfeng Cheng, for their kindly comments on my work and help on my study. I also thank Prof. Sebastian Diehl, Prof. Andrea Gambassi, Prof. Hannes Janssen, Prof. Michel Pleimling, and Dr. Lukas Sieberer for helpful discussions.

I want to thank people in our group, for their constructive suggestions. I thank our graduate program coordinator, Betty Wilkins, and program support technician, Katrina Loan. My thanks extend to our IT staff members including Roger Link and Travis Heath. I especially wish to thank Dr. Hiba Assi, Dr. Priyanka and Dr. Jacob Carroll for their careful critical reading of chapters in the dissertation.

I thank the the U. S. Department of Energy, since all those projects are supported by the

U. S. Department of Energy, Office of Basic Energy Sciences, Division of Materials Science and Engineering under Award DE-FG02-SC0002308

I would like to thank all my friends in my study and my life, practically to my roommates Chengyuan Wen, Wei Zhao, Xiangwen Wang and Wenchao Yang.

I am specially grateful to Jie Qu.

Finally, I express my thankfulness to my parents for their endless love.

Contents

List of Figures

List of Tables

Chapter 1

Introduction

1.1 Non-equilibrium physics

A system in thermal equilibrium can be characterized in such a way that its stationary state maximizes entropy (at fixed total energy), or minimizes free energy (at fixed temperature). It evolves through the accessible configurations according to the its stationary probability distribution. For example, in most realistic applications, systems are assumed to be coupled to an external heat bath and thus are described by the canonical ensemble, for which the stationary probability distribution $P(E)$ is given by the Boltzmann factor

$$P(E) = \frac{1}{Z}\exp(-E/k_B T), \tag{1.1}$$

where E is the system energy, T is the temperature of the heat bath, Z is the partition function, which provides a normalization factor for this probability distribution, and k_B is the Boltzmann constant. This ensemble can be used to describe the stationary distribution of these systems; however, detailed information about the relaxation forwards equilibrium not is not encoded. Therefore, there may exist multiple methods to successfully relax a system toward the same stationary state governed by the Boltzmann distribution, even if the accompanying dynamical properties can be quite different. A well-known example is that the Ising model can be simulated on a computer using either Glauber or Metropolis dynamical algorithms. Another important property of equilibrium models is that they always obey detailed balance. Therefore, the probability currents between pair of accessible configurations of the systems cancel each other so that there is direct reversibility between any two accessible mircostates in this situation.

On the other hand, non-equilibrium dynamical systems are defined by the violation of detailed balance in their microscopic processes [1]. The word "non-equilibrium" refers to situations for which there are non-vanishing net probability currents between different microstates. But even those non-equilibrium systems can reach stationary states, where the Boltzmann distribution may still hold and the concepts of equilibrium can still be applied. However, there exist systems far from equilibrium for which detailed balance is violated so strongly that the equilibrium physics approximation never becomes applicable. External particle or energy currents drive systems out of equilibrium. Yet, these systems can reach macroscopic stationary states which need continuous particle or energy supply. Therefore, detailed balance cannot be established in these non-equilibrium stationary states. Non-equilibrium phase transitions, which are obtained through adjusting some control parameter(s) in such non-equilibrium systems and separate distinct non-equilibrium stationary states, are not yet fully classified. A quite general way to investigate the dynamics at a non-equilibrium transition is to initialize the system with a configuration that is far from equilibrium and let it relax subsequently to its asymptotic stationary state [2], which is of the topic of our primary interest in this dissertation.

Another important topic prominent in many non-equilibrium systems is pattern formation in spatially extended settings. Roughly speaking, these are spatio-temporal features with characteristic wave vector q_0 and characteristic frequency ω_0. The origin of pattern formation can be intrinsic instabilities that arise when systems are brought away from their thermal equilibrium by changing the associated control parameter(s) beyond their instability threshold, or external noise. Theoretically, systems with control parameter(s) near the threshold can be described by simple equations with a universal form, namely the "amplitude equation." However, in situation far beyond the threshold, it is sometimes possible to use simple "phase equations" by perturbation of the original ideal periodic structures.

1.2 The complex Ginzburg-Landau equation

In this dissertation, we mainly focus on a stochastic non-linear partial differential equation, the cubic complex Ginzburg-Landau equation (CGL),

$$\partial A/\partial t = (\mu_r + i\mu_i)A + (\alpha_r + i\alpha_i)\nabla^2 A - (\beta_r + i\beta_i)|A|^2 A, \tag{1.2}$$

where A is a complex order parameter that measures the amount of broken symmetry of the system; μ_r indicates the deviation from the transition threshold; μ_i is a frequency shift; α_r and β_r represent the diffusion constant and the nonlinear saturation, which are both required to be positive; α_i and β_i measure the strength of linear and nonlinear dispersion effects, respectively. Various phenomena can be described by this equation at least on a qualitative level, such as second-order phase transitions, superfluidity, and superconductivity. It is also equivalent to the Gross-Pitaevskii equation with complex coefficients which has been proposed to capture the open system-dynamics of driven-dissipative Bose-Einstein condensation [3–5] if an additive complex noise term is also included in the equation, which will be discussed in detail in Chapter 2.

There exist mainly two different approaches to study this non-linear equation, either analytically or numerically. A general framework for describing and understanding the complex dynamics in this kind of systems using a field theory approach is discussed in Ref [6]. However, one can also try to solve this equation using numerical methods. We will present the dynamic behavior of the CGL from numerical studies first. The analytic approach will be covered in Chapter 2.

First of all, the symmetries that can be associated with this equation are time and space translations, spatial reflections and rotations, and global gauge symmetry. Therefore, in a certain phase away from the transition $\mu_r > 0$, one can rescale the time and space variables, as well as the complex field A according to these symmetries:

$$\begin{aligned} A' &= \sqrt{\frac{\beta_r}{\mu_r}} A e^{i\mu_i t}, \\ t' &= \mu_r t, \\ \boldsymbol{x}' &= \sqrt{\frac{\mu_r}{\alpha_r}} \boldsymbol{x}, \end{aligned} \tag{1.3}$$

and rewrite $A' \to A$, $\boldsymbol{x}' \to \boldsymbol{x}$, $t' \to t$, $\alpha_i/\alpha_r \to b$ and $\beta_i/\beta_r \to c$. A reduced form of the original CGL can be written in the form:

$$\partial A/\partial t = A + (1 + ib)\nabla^2 A - (1 + ic)|A|^2 A, \tag{1.4}$$

with only two real control parameters b and c left. This is the specific form that is usually employed in numerical investigations. It is known as an amplitude equation that describes “weekly nonlinear” spatiotemporal phenomena in the spatially extended case, especially for dimension $d = 1$ or 2. Furthermore, Eq. (1.4) is invariant upon the transformation $(A, b, c) \to (A^*, -b, -c)$. Therefore, only one half-plane in the (b, c) parameter space needs to be considered. This equation can be also viewed as an extension of the “real” time-dependent Ginzburg-Landau equation (RGL) [7]

$$\partial A/\partial t = A + \nabla^2 A - |A|^2 A \tag{1.5}$$

by setting $b = c = 0$, as well as of the nonlinear Schrödinger equation (NLS)

$$i\partial A/\partial t = \nabla^2 A \pm |A|^2 A \tag{1.6}$$

in the limit $b, c \to \infty$.

The simplest solutions of Eq. (1.4) are plane waves [7]:

$$\begin{aligned} A &= \sqrt{1-Q^2}\exp[i(\boldsymbol{Q}\cdot\boldsymbol{r} - \omega_p(Q)t + \phi)], \\ F^2 &= 1 - Q^2, \qquad \omega_p(Q) = c(1-Q^2) + bQ^2. \end{aligned} \tag{1.7}$$

Here ϕ is just a constant phase that can be chosen arbitrarily, due to the gauge symmetry. Furthermore, for plane waves the amplitude F should be a real number, thus this solution only exists for $Q^2 < 1$.

These most standard solutions are rarely observed in numerical studies, because of the spatiotemporal chaos that emerges prominently in CGL systems. Two different types of chaotic fluctuation are encountered: One is called "phase chaos" where only the phase of the complex order parameter A is dynamically active while the amplitude remains saturated. This phase chaos is also known as phase turbulence and has, e.g., been studied by Manneville and Chaté [8]. On the other hand, phase chaos can transition into a "defect chaos" state upon varying the control parameters (b, c) [9]. The term "defect" refers to topological defects, which are characterized by zeros of the complex field A, enforcing singularities of the phase $\theta = argA$. Specifically in two dimensions, these singular topological defects are points with integer topological charge $m = \oint_L \nabla\theta \boldsymbol{dl}/2\pi$, where L is a contour around the zero point of A, and m is used to quantify the singularity of the defect. Only single-charged defects with $m = \pm 1$ are stable. Multi-charged defects will successively split into single-charged defects [7]. The defect chaos, or "defect turbulence" state is then characterized by spontaneous creation and annihilation of opposite-charged topological defects.

More common spatio-temporal structures in the CGL in two dimensions are spiral waves, which are emitted by active topological defects. An isolated spiral solution was studied and described by Hagan [10]:

$$A(r, \theta, t) = F(r) \exp[i(-\omega t + m\theta + \psi(r))], \tag{1.8}$$

where (r, θ) are polar coordinates; m is the topological charge; ω is the rotation frequency of the spiral, $F(r)$ is the amplitude, and $\psi(r)$ is the position-dependent phase of the spiral, with the limiting forms:

$$\begin{aligned} F(r) &\rightarrow (1 - Q^2)^{\frac{1}{2}}, \psi' \rightarrow Q, \omega = (1 - Q^2)c + bQ^2, \text{ as } r \rightarrow \infty; \\ F(r) &\rightarrow ar^m, \psi' \rightarrow r, \text{ as } r \rightarrow 0. \end{aligned} \tag{1.9}$$

Hence the spiral wave solution will become plane-wave-like in the large-distance asymptotic limit $r \rightarrow \infty$.

Another set of important structures that are also associated with spiral waves are "shocks." In two dimensions, they are nearly hyperbolic line structures [11] that separate different spirals in space. As incoming fluctuations will be absorbed by these structures, there is no information communication between different spirals. Those spiral structures, together with shocks, eventually occupy the entire spatial domain, decimating all the defect turbulence. Consequently,the dynamics becomes frozen, and this final state is called the "frozen" state which is considered to persist indefinitely. However, there also exist active dynamical states where spirals behave similarly to vortices in the dynamical XY model. In that regime, spirals maintain an asymptotic wave length that is comparable to their typical extension; therefore, no significant shocks can form in this situation.

Above, we have briefly introduced the states of the CGL that we are predominantly interested in for this dissertation. We will further study these configurations in more detail in successive chapters. We will also discuss related physical phenomena and properties that we intend to investigate within the CGL framework.

1.3 Critical initial-slip and aging phenomena

The term "critical phenomena" is associated with the physics near a "critical point," where the characteristic correlation length diverges and relaxation processes slow down drastically. They are often considered to take place near continuous (second-order) phase transitions [6]. Dynamical scaling, as well as universality, are described by critical exponents and scaling functions. The "critical initial-slip" phenomenon emerges as the universal intermediate stage of a relaxation process towards criticality from a disordered non-equilibrium initial state. It is the crossover from the transient "initial-slip" to the asymptotic long-time regime that can be characterized by the dynamic critical exponent z. It displays universal behavior and can be (in some cases) described by a new independent critical exponent θ which emerges due to the fact that time translation symmetry is broken by the initial configuration. It was introduced and calculated by Janssen, Schaub, and Schmittmann [12] for an equilibrium non-conserved order parameter system (namely, model A, according to Hohenberg and Halperin's classification [13], or RGL with additive noise).

Physical aging phenomena, as introduced by Struik's [14] classical experimental study of the slow dynamics of certain glass-forming systems, are observed in various systems with slow relaxation dynamics [15]. They can be defined as follows: A physical system is considered to undergo aging if the relaxation process satisfies three properties: slow dynamics, for example, non-exponential decay; breaking of time-translation-invariance; dynamical scaling [16]. The simple aging scaling form of the two time autocorrelation function $C(t, s) = \langle \phi(t)\phi(s) \rangle$ is then given by:

$$C(t, s) = s^{-b} f_C(t/s), \;\; f_C(y) \sim y^{-\lambda_c/z}, \tag{1.10}$$

where ϕ is the order parameter and $s \ll t$ is called waiting time, b is the aging exponent while λ_C represents the autocorrelation exponent. The condition required for aging is very similar to that of a critical initial-slip. In fact, the initial-slip exponent and autocorrelation exponent can be connected by a scaling relation:

$$\lambda_C = d - \theta z \tag{1.11}$$

in the equilibrium model A case.

1.4 Classical nucleation theory

Nucleation is considered to be the first step in a spontaneous first-order transition, beginning with the metastability of the original initial state. It is generally suggested that there exists a finite kinetic barrier for a discontinuous transition. Nucleation processes strongly rely on rare events, the formation of "critical" nuclei, which describe the unstable state at the top of the barrier. Classical nucleation theory (CNT) is a simple intuitive model that was proposed around the middle of the 20th century [17, 18] and is described in detail in several reviews [19–22]. It provides a quantitative description and explanation of related phenomena based on appropriate approximations. The central result of CNT is a prediction of the nucleation rate

$$R = \rho Z j \exp\left(-\frac{\Delta F}{k_B T}\right), \tag{1.12}$$

where ΔF is the free energy cost of creating the critical nucleus, k_B is Boltzmann's constant and T is the absolute temperature, ρ is the number density of nucleation sites, j is the rate at which molecules attach to the nucleus, $Z < 1.0$ is the Zeldovich factor which describes the probability that a nucleus at the top of the barrier will proceed to form the new state. There are mainly two different kinds of nucleation: homogeneous nucleation which occurs in the bulk of a pure phase, and heterogeneous nucleation that is triggered by impurities or on surfaces. Homogeneous nucleation is much rarer than heterogeneous nucleation because the nucleation barrier is much lower in the heterogeneous case.

1.5 Structure of this thesis

This dissertation is structured as follows. In Chapter 1, we provide a general introduction to the model and phenomena that are studied in this thesis. An analytic study of the critical initial-slip scaling in the CGL is presented in Chapter 2. We then numerically solve the CGL on a two-dimensional square lattice. Using this approach, we investigate the associated scaling and aging phenomena when shock structures are absent in the system in Chapter 3 and the nucleation processes when the system is transiting from the strong fluctuating defect chaos state to a frozen state in Chapter 4. Finally, we provide an overall conclusion and outlook for this general research topic in Chapter 5.

Chapter 2

Critical initial-slip scaling for the noisy complex Ginzburg–Landau equation

This chapter is based on our publication [23]:

Liu, Weigang and Täuber, Uwe C, "Critical initial-slip scaling for the noisy complex Ginzburg–Landau equation," Journal of Physics A: Mathematical and Theoretical 49, 434001 (2016).

I performed all the numerical work under Dr. Uwe C. Täuber's supervision. All authors contributed to the analytical calculations and writing of this paper.

2.1 Introduction

Physical systems display characteristic singularities when their thermodynamic parameters approach a critical point. The ensuing singular behavior of various observables are governed by a considerable degree of universality: critical exponents and amplitude ratios are broadly independent of the microscopic details of the respective systems. The emergence of scale invariance, associated thermodynamic singularities, and universality near continuous phase transitions is theoretically understood and described by the renormalization group (RG), which also allows a systematic computation of critical exponents and associated scaling functions (see, e.g., Refs. [24–27]). These concepts and theoretical tools can be extended to dynamical critical behavior near equilibrium, which may similarly be grouped into various dynamical universality classes. In addition to global order parameter symmetries, the absence or presence of conservation laws for the order parameter and its coupling to other slow conserved modes crucially distinguish dynamical critical properties [6, 13, 28, 29]. More recently, dynamical RG methods have been utilized to characterize various continuous phase transitions far from thermal equilibrium as well [6, 30], including the associated universal short-time or 'initial-slip' relaxation features and 'aging' scaling [16]. Yet a complete classification of non-equilibrium critical points remains an open task.

Our study is in part motivated by recent experimental realizations of systems with strong light-matter coupling and a large number of degrees of freedom, which hold the potential of developing into laboratories for non-equilibrium statistical mechanics, and specifically for phase transitions among distinct non-equilibrium stationary states [31]. We mention a few but significant examples: In ensembles of ultra-cold atoms, Bose–Einstein condensates placed in optical cavities have allowed experimenters to achieve strong light-matter coupling and led to the realization of open Dicke models [32, 33]. The corresponding phase transition has been studied in real time, including the determination of an associated critical exponent [34].

Other platforms, which hold the promise of being developed into true many-body systems by scaling up the number of presently available building blocks in the near future, are arrays of microcavities [35–38] and also certain optomechanical setups [39–41]. Genuine many-body ensembles in this latter class have been realized in pumped semiconductor quantum wells placed inside optical cavities [42]. Here, non-equilibrium Bose–Einstein condensation of exciton-polaritons has been achieved [43–45], where the effective bosonic degrees of freedom result from the strong hybridization of cavity light and excitonic matter states [31, 46, 47].

Two essential ingredients are shared among these non-equilibrium systems [5]. First, they are strongly driven by external fields and undergo a series of internal relaxation processes [31]. The irreversible non-equilibrium drive and accompanying balancing dissipation complement the reversible Hamiltonian dynamics, and generate both coherent and dissipative dynamics on an equal footing, albeit originating from physically quite independent mechanisms. The additional irreversible terms cause manifest violations of the detailed-balance conditions characteristic of many-body systems in thermal equilibrium, and induce the break-down of the equilibrium Einstein relations that connect the relaxation coefficients with the thermal noise strengths. Second, the particle number in these systems is not conserved due to the coupling of the electromagnetic field to the matter constituents, thus opening strong loss channels for the effective hybridized light-matter degrees of freedom. The resulting quasi-particle losses must be compensated by continuous pumping in order to reach stable non-equilibrium stationary states.

Interestingly, detailed-balance violations generically turn out to be irrelevant for purely relaxational critical dynamics of a non-conserved order parameter in the vicinity of continuous phase transitions, which are hence characterized by the equilibrium model A universality class [48]. Yet in systems that undergo driven-dissipative Bose-Einstein condensation, an additional independent critical exponent associated with the non-equilibrium drive emerges, which describes universal decoherence at large length- and time scales; it was originally identified by means of a functional RG approach [3, 4], and subsequently computed within the perturbative RG framework [5]. This novel decoherence exponent should be observable in the momentum- and frequency-resolved single-particle response that may, e.g., be probed in homodyne detection of exciton-polaritons [49].

In $d > 2$ dimensions, the effective dynamical description or driven-dissipative Bose condensates utilizes a stochastic Gross–Pitaevskii equation with complex coefficients [3, 4], or, equivalently, a complex time-dependent Ginzburg–Landau equation that generalizes the equilibrium 'model A' relaxational kinetics [5]. The latter also features very prominently in the mathematical description of spontaneous spatio-temporal pattern formation in driven non-equilibrium systems [50, 51], and appears, for example, in the stochastic population dynamics for three cyclically competing species (May–Leonard model without particle number conservation) and related spatially extended evolutionary game theory systems [52]. Its critical properties have previously been investigated in the context of coupled driven non-linear oscillators that undergo a continuous synchronization transition at a Hopf bifurcation instability [53]. Intriguingly, however, two-dimensional driven-dissipative Bose–Einstein condensation appears to be captured by an anisotropic variant of the Kardar–Parisi–Zhang stochastic partial differential equation [54].

An alternative and powerful method to extract dynamical critical exponents and identify dynamical universality classes proceeds through the analysis of non-equilibrium relaxation processes and the ensuing critical aging scaling [12, 16]. To this end, one prepares the system initially in a fully disordered state with vanishing order parameter, and studies its subsequent relaxation towards equilibrium or stationarity. The initial preparation breaks time translation invariance; if the system is quenched near a critical point, the resulting critical slowing-down renders relaxation times huge, whence the transient non-stationary aging regime extends for very long time intervals, and this critical initial-slip regime is governed by universal power laws [12, 55]. In the case of a non-conserved order parameter or equilibrium model A in the terminology of Halperin and Hohenberg [13], this process is in fact characterized by an independent critical initial-slip exponent θ and an associated universal scaling function with a single non-universal scale factor [12]. We remark that the original perturbative RG treatment for the critical universal short-time dynamics and aging scaling has only just been extended towards a non-perturbative numerical analysis [56].

In contrast to model A relaxational kinetics, for dynamical critical systems with a conserved order parameter, the aging scaling regime is entirely governed by the long-time asymptotic stationary dynamical scaling exponents [12]; this is true also for models that incorporate couplings to other slow conserved fields [57, 58]. Consequently, the initial-slip or aging scaling regime provides a convenient means to quantitatively characterize critical dynamics in numerical simulations (and presumably real experiments as well) during the system's non-equilibrium relaxation phase [59]. Non-equilibrium critical relaxation and aging scaling has also been explored in driven systems that either display generic scale invariance, or are tuned at a continuous phase transition point. Prominent examples include the Kardar–Parisi–Zhang equation for driven interfaces or growing surfaces [60–62], driven diffusive systems [61, 63], and reaction-diffusion or population dynamics models that display a transition to an absorbing state, e.g., in the contact process [64], and stochastic spatially extended Lotka–Volterra models for predator-prey competition, for which the emergence of aging scaling may serve as an early-time indicator for the predator species extinction [65].

Inspired by these significant findings, in this present work we address the question if the universal non-equilibrium relaxation processes in the critical complex time-dependent Ginzburg–Landau equation differ from the corresponding equilibrium dynamical model A ? In order to attack this problem mathematically, we utilize the path integral representation of stochastic

Langevin equations through a Janssen–De Dominicis functional [6, 66–68], as previously developed and analyzed in the critical stationary regime for driven-dissipative Bose–Einstein condensation in Ref. [5]. Following Ref. [12] for the initial-slip and aging scaling analysis of the relaxational models A and B in thermal equilibrium, we represent the randomized initial state through a Gaussian distribution for the complex-valued order parameter field. We then employ the perturbative field-theoretical RG approach [24–27], and specifically its extension to critical dynamics [6, 28, 29], to analyze the ensuing singularities and compute the critical exponents. Since the initial conditions at time $t = 0$ may be viewed as specifying sharp boundary conditions on the semi-infinite time sheet, one can borrow theoretical tools originally developed for the investigation for surface critical phenomena [69]. Near and below the upper critical dimension $d_c = 4$, the parameter $\epsilon = 4 - d$ serves as the effective small expansion parameter for the ensuing perturbation series in terms of non-linear fluctuation loops.

The bulk part of this paper is organized as follows: In the following section 2.2, we provide the mesoscopic dynamical model based on a stochastic Gross–Pitaevskii partial differential equation with complex coefficients that is motivated by experimental studies on driven-dissipative Bose–Einstein condensation [3, 4]. Equivalently, this non-equilibrium kinetics can be viewed as relaxational model A dynamics of a non-conserved complex order parameter field orginating from a complex-valued Landau–Ginzburg functional [5]. Then, utilizing the harmonic Feynman diagram components, i.e., correlation and response propagators that are constructed from the linear part of the associated Janssen–De Dominicis response functional [12], we first discuss the system's dynamics on the mean-field level, including the fluctuation-dissipation ratio [55]. Section 2.3 details our perturbative RG calculation to lowest non-trivial (one-loop) order in ϵ. Upon utilizing a additional renormalization constant for the order parameter field on the 'initial-time sheet,' we obtain the scaling behavior of our model and determine the additional independent initial-slip critical exponent associated with a fully randomized initial state [12]. Through the extra renormalization constant acquired by the initial preparation that induces breaking of time translation invariance, we extract the initial-slip exponent which governs the universal short-time behavior as well as the non-equilibrium relaxation in the aging scaling regime. We then proceed to discuss the resulting two-loop and higher-order corrections through numerical solutions of the one-loop RG flow equations for the non-linear coupling parameters [5] in section 2.4. In section 2.5, we construct a suitable complex spherical model A extension akin to Ref. [70] to provide an alternative demonstration for our main conclusion, namely that the critical aging scaling in the non-equilibrium complex Ginzburg–Landau equation is asymptotically governed by the equilibrium model A initial-slip exponent. We finally summarize our work in the concluding section 2.6. A brief appendix lists the fundamental momentum loop integrals evaluated by means of the dimensional regularization technique that are required for the perturbative renormalization group calculations.

2.2 Model description and mean-field analysis

Following Refs. [3–5], we employ a noisy Gross–Pitaevskii equation with complex coefficients to capture the dynamics of a Bose–Einstein condensate subject to dissipative losses and compensating external drive:

$$i\partial_t \psi(\boldsymbol{x},t) = \Big[-(A-iD)\nabla^2 - \mu + i\chi + (\lambda - i\kappa)|\psi(\boldsymbol{x},t)|^2\Big]\psi(\boldsymbol{x},t) + \zeta(\boldsymbol{x},t)\,. \tag{2.1}$$

Obviously, eq. (2.1) coincides with the time-dependent complex Ginzburg–Landau equation, which has been prominently employed to describe pattern formation in non-equilibrium systems in the noise-free deterministic limit [50, 51]. The complex bosonic field ψ here represents the polariton degrees of freedom. The complex coefficients have clear physical meanings as well: $\chi = (\gamma_p - \gamma_l)/2$ is the net gain, the balance of the incoherent pump rate γ_p and the local single-particle loss rate γ_l. The positive parameters λ and κ represent the two-body loss and interaction strength, respectively; and $A = 1/2m_{\text{eff}}$ relates to the quasi-particle effective mass. This stochastic partial differential equation is often not presented with an explicit diffusion coefficient D, whereas a frequency-dependent pump term $\sim \eta\partial_t\psi$ is added on its left-hand side [71, 72], whereupon eq. (2.1) is recovered through dividing by $1 - i\eta$ on both sides, i.e., with $D = A\eta$ and a subleading correction to the other coefficients, which are complex to begin with. Due to the freedom of normalizing the time derivative term as above in the equation of motion, this model accurately captures the physics close to the phase transition, since it describes the most general low-frequency dynamics in a systematic derivative expansion that incorporates all relevant coupling in dimensions $d > 2$ [5]. The complex Gaussian white noise term ζ can be entirely characterized through its correlators

$$\begin{aligned}
\langle \zeta^*(\boldsymbol{x}, t)\rangle &= \langle \zeta(\boldsymbol{x}, t)\rangle = 0\,, \\
\langle \zeta^*(\boldsymbol{x}, t)\zeta(\boldsymbol{x'}, t')\rangle &= \gamma\delta(\boldsymbol{x} - \boldsymbol{x'})\delta(t - t')\,, \\
\langle \zeta^*(\boldsymbol{x}, t)\zeta^*(\boldsymbol{x'}, t')\rangle &= \langle \zeta(\boldsymbol{x}, t)\zeta(\boldsymbol{x'}, t')\rangle = 0\,.
\end{aligned} \tag{2.2}$$

As mentioned above, the parameters A, D, λ, and κ should all be positive for physical stability. On the other hand, the coefficient χ starts out negative initially and becomes positive as the system undergoes a continuous driven Bose–Einstein condensation transition, which results in a non-vanishing expectation value $\langle \psi(\boldsymbol{x}, t)\rangle \neq 0$. The parameter μ, which can be considered as an effective chemical potential, needs to stay fixed as a requirement for stationarity. The Langevin equation (2.1) may be obtained from a microscopic description in terms of a quantum master equation upon employing canonical power counting in the vicinity of the critical point [3, 4, 73]. For analytical convenience, we introduce the following ratios to rewrite the Gross–Pitaevskii equation:

$$r = -\frac{\chi}{D}\,,\ r' = -\frac{\mu}{D}\,,\ u' = \frac{6\kappa}{D}\,,\ r_K = \frac{A}{D}\,,\ r_U = \frac{\lambda}{\kappa}\ . \tag{2.3}$$

Factoring out iD on the right-hand side of (2.1), and $i\kappa$ in front of the non-linear term, we arrive at the equivalent stochastic partial differential equation

$$\begin{aligned} \partial_t \psi(\boldsymbol{x},t) &= -D\Big[r + ir' - (1+ir_K)\nabla^2 + \frac{u'}{6}(1+ir_U)|\psi(\boldsymbol{x},t)|^2\Big]\psi(\boldsymbol{x},t) \\ &\quad +\xi(\boldsymbol{x},t) = -D\frac{\delta \bar{H}[\psi]}{\delta\psi^*(\boldsymbol{x},t)} + \xi(\boldsymbol{x},t)\,. \end{aligned} \tag{2.4}$$

The stochastic noise term $\xi = -i\zeta$ can be characterized similarly as ζ above. In the second line, we have written eq. (2.4) in the form of purely relaxational kinetics with a non-Hermitean effective 'pseudo-Hamiltonian'

$$\begin{aligned} \bar{H}[\psi] &= \int d^d x\,\Big[(r+ir')|\psi(\boldsymbol{x},t)|^2 + (1+ir_K)|\nabla\psi(\boldsymbol{x},t)|^2 \\ &\quad + \frac{u'}{12}(1+ir_U)|\psi(\boldsymbol{x},t)|^4\Big]\,. \end{aligned} \tag{2.5}$$

With the above assumptions, we can construct the equivalent dynamical Janssen–De Dominicis response functional [66–68] of this driven-dissipative model by introducing a Martin–Siggia–Rose response field $\tilde{\psi}(\boldsymbol{x},t)$ to average the stochastic noise ξ through a Gaussian integral; see, e.g., Ref. [6] for more detailed explanations:

$$\begin{aligned} A[\tilde{\psi},\psi] \;=\; \int d^dx \int dt \, \Big\{ & \tilde{\psi}^*(\boldsymbol{x},t)\Big[\partial_t + D\Big(r + ir' - (1+ir_K)\nabla^2\Big)\Big]\psi(\boldsymbol{x},t) \\ & + \tilde{\psi}(\boldsymbol{x},t)\Big[\partial_t + D\Big(r - ir' - (1-ir_K)\nabla^2\Big)\Big]\psi^*(\boldsymbol{x},t) \\ & - \frac{\gamma}{2}|\tilde{\psi}(\boldsymbol{x},t)|^2 + D\frac{u'}{6}(1+ir_U)\tilde{\psi}^*(\boldsymbol{x},t)|\psi(\boldsymbol{x},t)|^2\,\psi(\boldsymbol{x},t) \\ & + D\frac{u'}{6}(1-ir_U)\tilde{\psi}(\boldsymbol{x},t)|\psi(\boldsymbol{x},t)|^2\,\psi^*(\boldsymbol{x},t) \Big\} \, . \end{aligned} \tag{2.6}$$

In addition to this bulk action [5], we must specify randomized initial configurations at the $t = 0$ time sheet from which the system relaxes. To this end, we assume a Gaussian weight for the initial order parameter field characterized by $\langle \psi(\boldsymbol{x},0) \rangle = a(\boldsymbol{x})$ at the initial time surface. In addition to taking averages with the bulk weight $\exp(-A[\tilde{\psi},\psi])$, we then require averaging with the Gaussian probability distribution

$$e^{-H_i[\psi]} = \exp\left[-\Delta \int d^dx \, |\psi(\boldsymbol{x},0) - a(\boldsymbol{x})|^2\right] , \tag{2.7}$$

which specifies an initial state with mean spatially varying order parameter $a(\boldsymbol{x})$ and the correlations

$$\Big\langle \big[\psi(\boldsymbol{x},0) - a(\boldsymbol{x})\big]\big[\psi^*(\boldsymbol{x'},0) - a^*(\boldsymbol{x'})\big] \Big\rangle = \Delta^{-1}\delta(\boldsymbol{x} - \boldsymbol{x'}) \, . \tag{2.8}$$

We now set $\psi(\boldsymbol{x}, t < 0) = 0$, whereupon the Gaussian part of the action (2.6) becomes

$$\begin{aligned} A_0[\tilde{\psi},\psi] = \int d^dx \int_0^\infty dt \, \Big\{ & \tilde{\psi}^*(\boldsymbol{x},t)\Big[\partial_t + D\Big(r + ir' - (1+ir_K)\nabla^2\Big)\Big]\psi(\boldsymbol{x},t) \\ & + \tilde{\psi}(\boldsymbol{x},t)\Big[\partial_t + D\Big(r - ir' - (1-ir_K)\nabla^2\Big)\Big]\psi^*(\boldsymbol{x},t) - \frac{\gamma}{2}|\tilde{\psi}(\boldsymbol{x},t)|^2 \Big\}. \end{aligned} \tag{2.9}$$

We finally complement the action with external source terms J and $\tilde{J}$ conjugate to both the

ψ and $\tilde{\psi}$ fields:

$$\begin{aligned} A_J[\tilde{\psi},\psi] \;\; &= \;\; -\int d^dx \int dt \, \Big[\tilde{J}^*(\boldsymbol{x},t)\tilde{\psi}(\boldsymbol{x},t) + J^*(\boldsymbol{x},t)\psi(\boldsymbol{x},t) \\ &\qquad + \tilde{J}(\boldsymbol{x},t)\tilde{\psi}^*(\boldsymbol{x},t) + J(\boldsymbol{x},t)\psi^*(\boldsymbol{x},t) \Big] \, . \end{aligned} \tag{2.10}$$

Hence, the ultimate generating functional of our model becomes

$$\mathcal{Z}[\tilde{J},J] = \int \mathfrak{D}[i\tilde{\psi}] \int \mathfrak{D}[\psi] \, \exp\Big[- \left(A[\tilde{\psi},\psi] + H_i[\psi] + A_J[\tilde{\psi},\psi] \right) \Big] \, . \tag{2.11}$$

We first analyze the mean-field theory for our model. By means of the Green's function technique, we may directly solve the classical field equations for the Gaussian generating functional $\mathcal{Z}_0[\tilde{J},J]$ to obtain the mean-field expressions for the expectation values $\langle \tilde{\psi}(\boldsymbol{x},t) \rangle_0$ and $\langle \psi(\boldsymbol{x},t) \rangle_0$:

$$\begin{aligned} 0 = \frac{\delta(A_0 + H_i + A_J)}{\delta\tilde{\psi}^*(\boldsymbol{x},t)} \;\; &= \;\; \Big[\partial_t + D\Big(r + ir' - (1+ir_K) \Big) \nabla^2 \Big] \psi(\boldsymbol{x},t) \\ &\qquad - \tilde{J}(\boldsymbol{x},t) - \frac{\gamma}{2} \tilde{\psi}(\boldsymbol{x},t) \, , \\ 0 = \frac{\delta(A_0 + H_i + A_J)}{\delta\psi^*(\boldsymbol{x},t)} \;\; &= \;\; \Big[-\partial_t + D\Big(r - ir' - (1-ir_K) \Big) \nabla^2 \Big] \tilde{\psi}(\boldsymbol{x},t) \\ &\qquad - J(\boldsymbol{x},t) - \tilde{\psi}(\boldsymbol{x},0)\delta(t) + \Delta[\psi(\boldsymbol{x},0) - a(\boldsymbol{x})]\delta(t) \, . \end{aligned} \tag{2.12}$$

The integration limit for the differential equations above is constrained to $0 < t < \infty$, and the boundary conditions for the Martin–Siggia–Rose response field $\tilde{\psi}(\boldsymbol{x},t=0) = \Delta[\psi(\boldsymbol{x},0) - a(\boldsymbol{x})]$ and $\tilde{\psi}(\boldsymbol{x},t\to\infty) = 0$ are necessary to satisfy the initial distribution of $\psi(\boldsymbol{x},0)$. Solving these time differential equations in momentum space, we find for $\langle \tilde{\psi}(\boldsymbol{q},t) \rangle_0$ and $\langle \psi(\boldsymbol{q},t) \rangle_0$ in terms of the conjugate sources:

$$\begin{aligned}
\langle\tilde{\psi}(\boldsymbol{q},t)\rangle_0 &= \int_0^\infty \exp\Big\{D\Big[r-ir'+(1-ir_K)q^2\Big](t-t')\Big\}\,\Theta(t-t')J(\boldsymbol{q},t')\,dt'\,, \\
\langle\psi(\boldsymbol{q},t)\rangle_0 &= \int_0^\infty \exp\Big\{-D\Big[r+ir'+(1+ir_K)q^2\Big](t-t')\Big\}\,\Theta(t-t') \\
&\qquad \times\Big[\tilde{J}(\boldsymbol{q},t)+\frac{\gamma}{2}\tilde{\psi}(\boldsymbol{x},t)+\big[a(\boldsymbol{q})+\Delta^{-1}\tilde{\psi}(\boldsymbol{q},t)\big]\delta(t)\Big]\,dt'\,. \qquad (2.13)
\end{aligned}$$

Thus we determine the Gaussian response and correlation propagators $G^0_{\tilde{\psi}^*\psi}(\boldsymbol{q},t,t')=\langle\psi^*(\boldsymbol{q},t)\,\tilde{\psi}(\boldsymbol{q},t')\rangle = \delta\langle\tilde{\psi}(\boldsymbol{q},t')\rangle/\delta J(\boldsymbol{q},t)|_{J=\tilde{J}=0}$ and $C^0_{\psi^*\psi}(\boldsymbol{q},t,t') = \langle\psi^*(\boldsymbol{q},t')\psi(\boldsymbol{q},t)\rangle = \delta\langle\psi(\boldsymbol{q},t)\rangle/\delta\tilde{J}(\boldsymbol{q},t')\,|_{J=\tilde{J}=0}$, which serve as the basic components for the perturbation expansion and Feynman diagrams. By means of the expressions (2.13), we arrive at

$$G^0_{\tilde{\psi}^*\psi}(\boldsymbol{q},t,t') = G^0_{\tilde{\psi}^*\psi}(\boldsymbol{q},t-t') = e^{-D[r+ir'+(1+ir_K)q^2](t-t')}\,\Theta(t-t')\,, \qquad (2.14)$$

$$C^0_{\psi^*\psi}(\boldsymbol{q},t,t') = C^D_{\psi^*\psi}(\boldsymbol{q},t,t')+\Delta^{-1}G^0_{\tilde{\psi}^*\psi}(\boldsymbol{q},t)G^0_{\tilde{\psi}\psi^*}(\boldsymbol{q},t')\,. \qquad (2.15)$$

Comparing with the bulk propagators of Ref. [5], the harmonic response propagator (2.14) here is not influenced by the initial condition and remains translationally invariant in time, whereas the correlation propagator (2.15), more precisely, its Dirichlet component $C^D_{\psi^*\psi}(\boldsymbol{q},t,t')$, distinctly reflects the initial preparation and does not obey time translation invariance,

$$C^D_{\psi^*\psi}(\boldsymbol{q},t,t') = \frac{\gamma\, e^{-iD(r'+r_Kq^2)(t-t')}}{4D(r+q^2)}\Big[e^{-D(r+q^2)|t-t'|}-e^{-D(r+q^2)(t+t')}\Big]\,. \qquad (2.16)$$

Under RG scale transformations, the initial configuration distribution width Δ is a relevant parameter, and one expects $\Delta\to\infty$ under the renormalization group flow [12]. If this asymptotic limit $\Delta\to\infty$ is taken, the second term in $C^0_{\psi^*\psi}(\boldsymbol{q},t,t')$ becomes eliminated, and we are left with only the Dirichlet correlator (2.16).

It is instructive to follow Ref. [55], and use the Gaussian response and correlation propagators to evaluate the fluctuation-dissipation ratio

$$X(\boldsymbol{q}; t > t', t') = k_{\mathrm{B}}T \, \frac{\chi(\boldsymbol{q}; t > t', t')}{dC^0_{\psi^*\psi}(\boldsymbol{q}; t, t')/dt'} \, . \tag{2.17}$$

In thermal equilibrium, this ratio is required to be 1 according to Einstein's relation. To this end, we require the dynamic susceptibility or response function

$$\chi(\boldsymbol{q}; t > t', t') = D(1 + ir_K) \, G^0_{\tilde{\psi}^*\psi}(\boldsymbol{q}, t, t') \, , \tag{2.18}$$

wherefrom we obtain the inverse fluctuation-dissipation ratio (2.17) in momentum space for our model

$$\begin{aligned} X(\boldsymbol{q}; t > t', t')^{-1} = \frac{\gamma}{4Dk_{\mathrm{B}}T(r + q^2)(1 + ir_K)} \Big[r + ir' + (1 + ir_K)q^2 \\ + (r - ir' + q^2 - ir_K q^2) \, e^{-2D(r+q^2)t'} \Big] - \frac{r - ir' + (1 - ir_K)q^2}{\Delta(1 + ir_K)} \, e^{-2D(r+q^2)t'} \, . \end{aligned} \tag{2.19}$$

In the asymptotic time limit $t' \to \infty$, this expression reduces to

$$\lim_{t' \to \infty} X(\boldsymbol{q}; t > t', t')^{-1} = \frac{\gamma[r + ir' + (1 + ir_K)q^2]}{4Dk_{\mathrm{B}}T(r + q^2)(1 + ir_K)} \, . \tag{2.20}$$

In order to satisfy the fluctuation-dissipation theorem as required for the system to relax towards thermal equilibrium at long times, one must thus demand the following relationships between the parameters in the modified Gross–Pitaevskii or complex time-dependent Ginzburg–Landau equation (2.4):

$$r' = r_K r \, , \ \gamma = 4Dk_{\mathrm{B}}T \, . \tag{2.21}$$

In the critical regime $r = r' = 0$ and $q^2 = 0$, where the characteristic relaxation time scale $t_c = [D(r+q^2)]^{-1}$ diverges, the fluctuation-dissipation ratio (2.19) will never reach the thermal equilibrium limit 1; in fact even with equilibrium parameters (2.21) it attains a fixed complex value at any time t',

$$X(0; t > t', t') = \frac{1 + ir_K}{2} \,. \tag{2.22}$$

In the asymptotic Dirichlet limit $\Delta \to \infty$, the fluctuation-dissipation ratio becomes in real space

$$\begin{aligned} X_0(\boldsymbol{x}; t > t', t')^{-1} = 1 + \frac{1 - ir_K}{1 + ir_K} & \left(\frac{t - t'}{t + \frac{1 - ir_K}{1 + ir_K}\, t'} \right)^{d/2} \\ & \times \exp\left(-2Dt' \left[r - \frac{x^2}{4D^2 (t - t')(1 + ir_K)^2 \bigl(t + \frac{1 - ir_K}{1 + ir_K}\, t'\bigr)} \right] \right) . \end{aligned} \tag{2.23}$$

This result yields the corresponding equilibrium model A expression for $r_K = 0$ [55]. In the long-time limit $t, t' \to \infty$, with the time ratio $s = t'/t$ held fixed, we find near the critical point $r = 0$,

$$X_0(0; s = t'/t < 1)^{-1} = 1 + \frac{1 - ir_K}{1 + ir_K} \left(\frac{1 - s}{1 + \frac{1 - ir_K}{1 + ir_K} s} \right)^{d/2} . \tag{2.24}$$

Thermal equilibrium is restored as $s \to 1$. However, for $s = 0$ the ratio (2.22) is reached: $X_0(0; 0)^{-1} = 1 + (1 - ir_K)/(1 + ir_K)$. This suggests a crossover between the time ratio regimes $s = 1$ and $s = 0$, which can be associated with the critical initial slip exponent θ. In the following section, we shall write down the associated general scaling laws, and explicitly calculate θ for our specific model by means of the perturbative dynamical RG to one-loop order, or first order in the dimensional expansion in $\epsilon = 4 - d$.

2.3 Renormalization group analysis to one-loop order

As established by Janssen, Schaub, and Schmittmann, the general scaling form in the initial-slip or critical aging regime $t' \ll t$ for the dynamical correlation function of the equilibrium model A for a non-conserved order parameter with purely relaxational kinetics reads

$$C(\boldsymbol{q}; t, t'/t \to 0) = |\boldsymbol{q}|^{-2+\eta} \, (t/t')^{\theta-1} \, \hat{C}_0(\boldsymbol{q}\xi, |\boldsymbol{q}|^z Dt) \, , \tag{2.25}$$

where $\xi \sim |\tau|^{-\nu}$ denotes the diverging correlation length as the critical point at $\tau = 0$ is approached, with associated critical exponent ν; z indicates the dynamical critical exponent that describes critical slowing-down, while θ denotes the universal initial-slip exponent θ [12]. In thermal equilibrium, the fluctuation-dissipation theorem then yields the corresponding scaling form for the dynamic susceptibility:

$$\chi(\boldsymbol{q}; t, t'/t \to 0) = D|\boldsymbol{q}|^{z-2+\eta} \, (t/t')^{\theta} \, \hat{\chi}_0(\boldsymbol{q}\xi, |\boldsymbol{q}|^z Dt) \, \Theta(t) \, . \tag{2.26}$$

For the driven-dissipative Gross–Pitaevskii equation or complex Ginzburg–Landau equation, the following more general scaling form applies for the dynamical response function [5]:

$$\begin{aligned} \chi(\boldsymbol{q}; t, t'/t \to 0) \;&=\; D|\boldsymbol{q}|^{z-2+\eta} \, (1 + ia|\boldsymbol{q}|^{\eta-\eta_c})^{-1} \, (t/t')^{\theta} \\ &\quad \times \hat{\chi}_0\Big(\boldsymbol{q}\xi, |\boldsymbol{q}|^z (1 + ia|\boldsymbol{q}|^{\eta-\eta_c}) Dt\Big) \Theta(t) \, . \end{aligned} \tag{2.27}$$

Here, the universal correction-to-scaling exponent η_c is induced by the external drive, and describes the ultimate disappearance of coherent quantum fluctuations at the critical point relative to the dissipative internal noise. To second order in the dimensional expansion, one obtains $\eta_c = -[4 \ln(4/3) - 1 + O(\epsilon)]\eta$. Similar additional terms apply to the dynamical correlation function (2.25), albeit in general with also modified Fisher exponent $\eta \to \eta'$ and

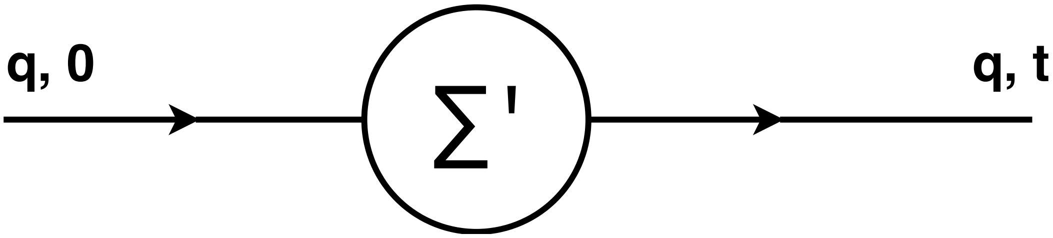

Figure 2.1: Full response propagator and one-particle reducible self-energy.

initial-slip exponent $\theta \to \theta'$:

$$C(\boldsymbol{q}; t, t'/t \to 0) = |\boldsymbol{q}|^{-2+\eta'} \, (t/t')^{\theta'-1} \, \hat{C}_0(\boldsymbol{q}\xi, |\boldsymbol{q}|^z D t, a|\boldsymbol{q}|^{\eta-\eta_c}) \, . \tag{2.28}$$

Yet both the perturbative and non-perturbative RG analysis have established that this system eventually thermalizes in the critical regime, whereupon detailed balance becomes effectively restored. This thermalization, which requires that $\Delta = r_U - r_K \to 0$, implies the identities $\eta' = \eta$ and also $\theta' = \theta$. In addition, asymptotically in fact $r_U = r_K \to 0$ and hence also $r' \to 0$, whereupon eq. (2.4) turns into the equilibrium time-dependent Ginzburg–Landau equation with a non-conserved complex order parameter field. Consequently the static and dynamic critical exponents ν, η, and z all become identical to those for the two-component equilibrium model A [3–5].

This leaves us with the explicit computation of the initial-slip or critical aging exponent θ for our driven-dissipative system, for which we may closely follow the procedure in Ref. [12]. Hence we just sketch the essential points in this calculation. The first step is to list the basic components for the perturbation series and associated Feynman diagrams. The response (2.14) and correlation propagators (2.15) are already listed above, and are graphically represented by directed and non-directed lines, respectively. The non-linear fluctuation terms

$\propto u'$ in the Janssen–De Dominicis functional (2.6) yield the four-point vertex

$$-\frac{1}{2}\Gamma^0_{\tilde{\psi}\psi^*\psi^*\psi} = -D\frac{u'}{6}\,(1+ir_U) \tag{2.29}$$

and its complex conjugate. The randomized initial preparation of the system breaks time translation invariance, and induces one additional singularity that needs to be renormalized on the initial time sheet in the temporal domain. Inspection of the ensuing Feynman graphs for the response propagator shows that it can generally be written as a convolution of its stationary counterpart and a one-particle reducible self-energy Σ', see Fig. 2.1; i.e.:

$$\langle\psi(-\boldsymbol{q},t)\tilde{\psi}^*(\boldsymbol{q},t)\rangle = \int_0^t \langle\psi(-\boldsymbol{q},t)\tilde{\psi}^*(\boldsymbol{q},t')\rangle_{\rm stat}\,\Sigma'(\boldsymbol{q},t')\,dt'\,. \tag{2.30}$$

To first order in u', the only contribution to Σ' is the 'Hartree loop' shown in Fig. 2.2. In the asymptotic limit $\Delta\to\infty$, it is to be evaluated with the Dirichlet correlator (2.16), which yields

$$\Sigma'(\boldsymbol{q},t) = \delta(t) - \frac{2}{3}u'D(1+ir_U)\,G^0_{\tilde{\psi}^*\psi}(\boldsymbol{q},t)\int\frac{d^dk}{(2\pi)^d}\,C^D_{\psi^*\psi}(\boldsymbol{k},t,t)\,. \tag{2.31}$$

It is crucial to note that as the loop closes onto itself at intermediate time t', the non-equilibrium component in the first term of eq. (2.16) that contains r' and r_K disappears, and the Dirichlet propagator contributions are identical to those in equilibrium. After straightforward temporal Fourier transform, we obtain after integration with dimensional regularization (see appendix A):

$$\begin{aligned}\Sigma'(\boldsymbol{q},\omega) \quad = \quad & 1+\frac{\gamma u'(1+ir_U)A_d}{6[(1+ir_U)r+(1+ir_K)q^2+i\omega/D](d-2)\epsilon} \\ & \times\frac{1}{[(3+ir_U)r/2+(1+ir_K)q^2/2+i\omega/2D]^{1-d/2}}\,,\end{aligned} \tag{2.32}$$

where $A_d = \Gamma(3-d/2)/2^{d-1}\pi^{d/2}$.

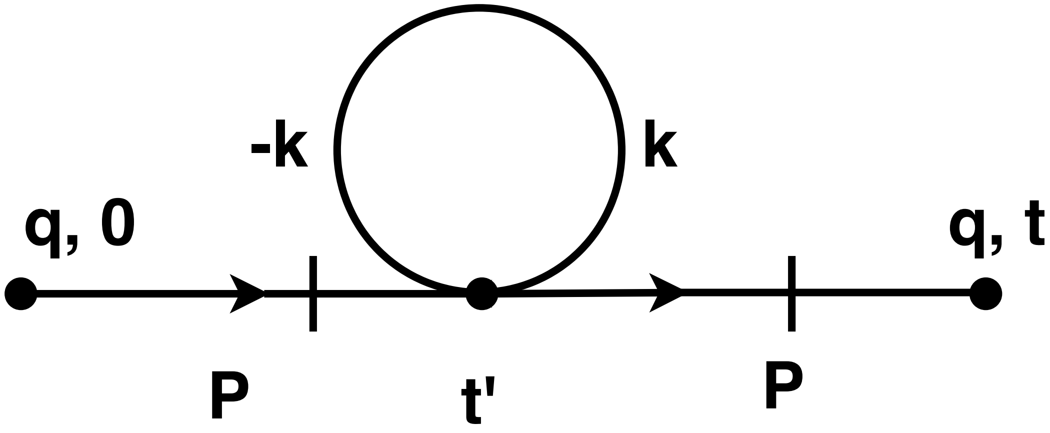

Figure 2.2: Feynman tadpole diagram or Hartree loop.

For the subsequent renormalization procedure, we set the normalization point to $r = 0$, $\boldsymbol{q} = 0$, but $i\omega/2D = \mu^2$ outside the infrared-singular region, whence in minimal subtraction and with (2.21) and $u = k_{\rm B}Tu'$:

$$\Sigma'(0,\omega)_{\rm NP} = 1 + \frac{u(1+ir_U)A_d\mu^{-\epsilon}}{3\epsilon}\,. \tag{2.33}$$

Next we define the renormalization constant for the initial response field through $\tilde{\psi_R}(\boldsymbol{x},0) = (Z_0 Z_{\tilde{\psi}})^{1/2}\tilde{\psi}(\boldsymbol{x},0)$, whence Z_0 absorbs the ultraviolet divergence in the renormalized self-energy: $\Sigma'_R(\boldsymbol{q},\omega) = Z_0^{1/2}\Sigma'(\boldsymbol{q},\omega)$. Explicitly, we then find to one-loop order

$$Z_0 = 1 - \frac{2u_R(1+ir_{UR})}{3\epsilon} + O(u_R^2)\,, \tag{2.34}$$

where $u_R = Z_u u A_d \mu^{-\epsilon}$ and $r_{UR} = Z_{r_U} r_U$ with Z_u and Z_{r_U} determined in Ref. [5]. The associated Wilson's flow function that enters the renormalization group equation becomes

$$\gamma_0(u_R) = \mu\partial_\mu|_0 \ln Z_0 = \frac{2}{3}\,u_R(1+ir_{UR}) + O(u_R^2)\,. \tag{2.35}$$

As a final step, one resorts to a short-time expansion for the response field $\tilde{\psi}(\boldsymbol{x}, t') = \tilde{\sigma}(t')\tilde{\psi}(\boldsymbol{x}, 0) + \ldots$, which through the RG flow translates into the asymptotic scaling $\tilde{\sigma}(t') = (Dt')^{-\theta}\hat{\sigma}(t'/\xi^z)$ [12], where we identify

$$\theta = \gamma_0(u^*)/2z\,. \tag{2.36}$$

Under the RG flow, as stated before, $r_{UR} \to 0$ [5], and the non-linear coupling u_R approaches an infrared-stable fixed point $u^* = 3\epsilon/5 + O(\epsilon^2)$ in dimensions $d < d_c = 4$ ($\epsilon > 0$). Thus $\gamma_0(u^*) = 2\epsilon/5 + O(\epsilon^2)$, and with the standard two-loop critical exponents for the equilibrium model A with two order parameter components [6, 29]

$$\eta = \epsilon^2/50 + O(\epsilon^3)\,, \quad z = 2 + [6\ln(4/3) - 1 + O(\epsilon)]\,\eta\,, \tag{2.37}$$

we at last obtain

$$\theta = \epsilon/10 + O(\epsilon^2)\ , \tag{2.38}$$

precisely as for the two-component model A.

2.4 Effect of two-loop and higher-order fluctuation corrections

Higher-order loop corrections assuredly do not display the temporally local feature of the tadpole graph, Fig. 2.2; hence non-equilibrium contributions and phase-coherent interference terms from the dynamical correlation functions (2.15) cause deviations relative to the relaxation kinetics in the equilibrium model A. However, we know from the one-loop RG flow equations that asymptotically all non-equilibrium parameters flow to zero [5]. Any effects

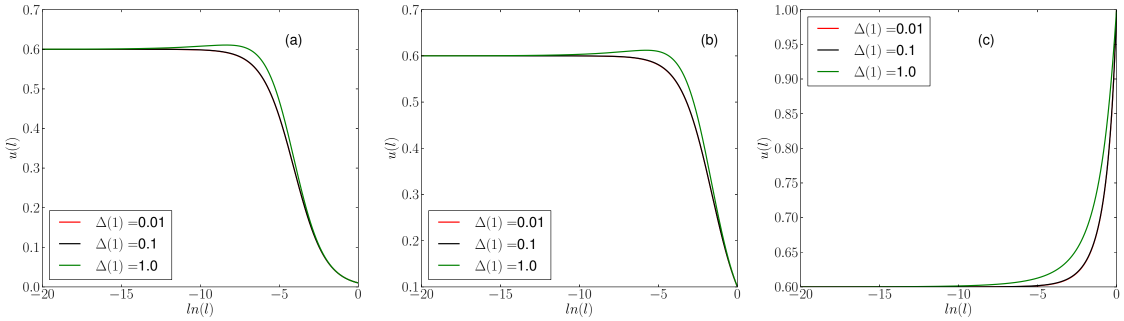

Figure 2.3: Flow of the non-equilibrium parameter $\Delta(\ell)$ with initial values (a) $\Delta(1) = 0.01$, (b) $\Delta(1) = 0.1$, and (c) $\Delta(1) = 1.0$ for several different initial values of the non-linear coupling $u(1) = 0.01,\ 0.1,\ 1.0$, in $d = 3$ dimensions ($\epsilon = 1$) and $r_k(1) = 1.0$.

from the coherent quantum kinetics thus ultimately disappear at the critical point, which also applies to the critical aging scaling regime. Yet for some initial values of the running couplings, conceivably the RG flow might temporarily reach a transient metastable point in parameter space, with associated dynamic scaling properties distinct from those of the two-component model A.

In order to investigate this possibility, we consider the one-loop RG flow equations for the running counterparts of the non-linear coupling u_R and the non-equilibrium parameter $\Delta_R = r_{UR} - r_{KR}$, as derived in Ref. [5]:

$$
\begin{aligned}
l\partial_l u(l) &= u(l)\left[-\epsilon + \frac{5}{3}\,u(l) - \frac{\Delta(l)^2}{3[1 + r_K(l)^2]}\,u(l) + O\big(u(l)^2\big)\right], \\
l\partial_l \Delta(l) &= \Delta(l)\left[1 + \frac{2r_K(l)\Delta(l) + \Delta(l)^2}{1 + r_K(l)^2}\right]\frac{u(l)}{3} + O\big(u(l)^2\big)\,,
\end{aligned}
\tag{2.39}
$$

obtained from the characteristics $\mu \to \mu l$. Their ultimately stable equilibrium fixed point is $\Delta^* = 0$ and $u^* = 3\epsilon/5 + O(\epsilon^2)$. We solve the coupled system of non-linear ordinary differential equations (2.39) numerically by means of a four-step Runge-Kutta method, for various initial values $u(l = 1)$ and $\Delta(l = 1)$.

For dimensional parameter $\epsilon = 1$, i.e., $d = 3$, the resulting RG flows of the coupling param-

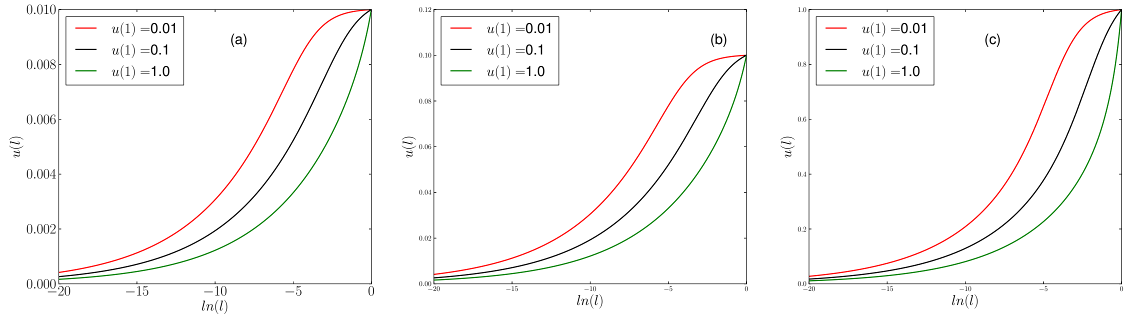

Figure 2.4: Flow of the non-linear coupling parameter $u(\ell)$ with initial values (a) $u(1) = 0.01$, (b) $u(1) = 0.1$, and (c) $u(1) = 1.0$ for several different initial values of the non-equilibrium parameter $\Delta(1) = 0.01,\ 0.1,\ 1.0$, in $d = 3$ dimensions ($\epsilon = 1$) and $r_k(1) = 1.0$.

eters $\Delta(l)$ and $u(l)$ are respectively shown in Figs. 2.3 and 2.4. We observe that the RG flow quite quickly runs into the asymptotic values $\Delta^* = 0$ and $u^* = 3/5$, which represents the equilibrium model A fixed point. No interesting transient metastable crossover region is discernible in these graphs for either parameter. This leads us to anticipate that the results from two- or higher-loop fluctuation corrections ultimately become identical to the corresponding ones for the two-component equilibrium model A [12], and no interesting distinct crossover region emerges.

2.5 Spherical model

Our goal in this section is to analyze the partition function $Z[h = 0]$ for an n-component extension of the complex Landau–Ginzburg pseudo-Hamiltonian in the spherical model limit $n \to \infty$, which can be directly generated from (2.5):

$$\begin{aligned} \bar{H}[\psi^\alpha] &= \int d^d x \Big[(r + ir') \sum_{\alpha=1}^{n} |\psi^\alpha(\boldsymbol{x})|^2 + (1 + ir_K) \sum_{\alpha=1}^{n} |\nabla \psi^\alpha(\boldsymbol{x})|^2 \\ &\qquad + \frac{u'}{12}(1 + ir_U) \Big(\sum_\alpha |\psi^\alpha(\boldsymbol{x})|^2 \Big)^2 \Big] . \end{aligned} \tag{2.40}$$

The corresponding spherical equilibrium model A has been investigated extensively in previous work, utilizing either a self-consistent decoupling method [12] or a Gaussian Hubbard–Stratonovich transformation to effectively 'linearize' the quartic non-linear term in this Hamiltonian (see, e.g., Refs. [6, 16, 70]). These two approaches are equivalent, but we employ the latter to analyze our non-equilibrium system. To this end, we introduce an auxiliary field $\Psi(\boldsymbol{x})$, through which the Gaussian Hubbard–Stratonovich transformation can be performed,

$$\int d(i\Psi)\, e^{-(1+ir_U)[\Psi(\sum_\alpha |\psi^\alpha|^2)-3\Psi^2/u']} \propto e^{-(1+ir_U)(\sum_\alpha |\psi^\alpha|^2)^2/12} \,. \tag{2.41}$$

Substituting this transformation as well as $r' = r_K r$, the augmented Hamiltonian becomes

$$\begin{aligned}\tilde{H}[\psi^\alpha, \Psi] \;&=\; \int d^d x \Big[(1+ir_K)[r+\Psi(\boldsymbol{x})] \sum_\alpha |\psi^\alpha(\boldsymbol{x})|^2 + (1+ir_K) \sum_\alpha |\nabla \psi^\alpha(\boldsymbol{x})|^2 \\ &\qquad -\frac{3}{u'}(1+ir_U)\Psi(\boldsymbol{x})^2\Big] \,.\end{aligned} \tag{2.42}$$

At this point the original order parameter fields can be integrated out, and one arrives at

$$Z[h=0] \;\propto\; \int \mathcal{D}[i\Psi] \exp\Big[\frac{3(1+ir_U)}{u'}\Psi(\boldsymbol{x})^2 - nTr \ln \frac{(1+ir_K)G_\Psi(\boldsymbol{x},\boldsymbol{x'})^{-1}}{2\pi}\Big], \tag{2.43}$$

with the inverse Green's function

$$G_\Psi(\boldsymbol{x},\boldsymbol{x'})^{-1} = [r + \Psi(\boldsymbol{x}) - \nabla^2]\, \delta(\boldsymbol{x}-\boldsymbol{x'}) \tag{2.44}$$

and its Fourier transform in momentum space

$$G_\Psi(\boldsymbol{q},\boldsymbol{q'})^{-1} = (r+q^2)\,(2\pi)^d \delta(\boldsymbol{q}+\boldsymbol{q'}) + \Psi(\boldsymbol{q}+\boldsymbol{q'}) \,. \tag{2.45}$$

Now recall that the RG fixed point for the non-linear coupling is $u^* \propto \epsilon/(n+2)$; thus, for large n, resetting the non-linear coupling as $u = u'/n$ will render the parameter u' independent of the number of components n as $n \to \infty$. This yields the partition function $Z[h=0] \propto \int \mathcal{D}[i\Psi] e^{-n\Phi[\Psi]}$ with the effective potential

$$\Phi[\Psi] = -\frac{3(1+ir_U)}{u'} \int d^d x \, \Psi^2(\boldsymbol{x}) + Tr \ln \frac{(1+ir_K) G_\Psi(\boldsymbol{x}, \boldsymbol{x'})^{-1}}{2\pi} \, . \tag{2.46}$$

In the spherical model limit $n \to \infty$, the steepest-descent approximation will become exact, that is we need to seek the solution of the classical field equation $\delta\Phi[\Psi]/\Psi(\boldsymbol{x}) = 0$. For simplicity, we assume a homogeneous solution $\Psi(\boldsymbol{x}) = \Psi$, whence the stationarity condition yields a self-consistent equation for Ψ:

$$\Psi = \frac{u'}{6(1+ir_U)} \int \frac{d^d q}{(2\pi)^d} \frac{1}{r + \Psi + q^2} \, . \tag{2.47}$$

This result looks precisely like its equibilirium spherical model A counterpart, aside from the overall complex prefactor $1+ir_U$. Specifically, the integral is just the bare correlation function $C_0(\boldsymbol{x}=0)$ with a shifted temperature parameter $r \to r+\Psi$. Yet previous work [6] established that asymptotically $r_U \to 0$ at the stable RG fixed point; therefore, one obtains the static critical exponents of the equilibrium spherical model A: $\eta = 0$ and $\gamma = 2\nu = 2/(d-2)$ for $d < d_c = 4$. Furthermore, the analysis for the dynamics of this non-equilibrium system will also be essentially identical as for the equilibrium spherical model [6, 16], and results in the dynamical critical and initial-slip exponents

$$z = 2 \, , \; \theta = (4-d)/4 \; , \tag{2.48}$$

both coinciding identical with the equilibrium spherical model A values.

The above analysis of the spherical model extension for the time-dependent complex Ginzburg–

Landau equation of course holds to all orders in a perturbative expansion. The fact that the spherical model limit too recovers the equilibrium values for all critical exponents of this system further supports our conclusion in the previous section 2.4 that higher-order fluctuation corrections to the critical initial-slip exponent for our driven non-equilibrium kinetics must be identical to those of model A in thermal equilibrium.

2.6 Conclusion and outlook

We have investigated the driven-dissipative non-equilibrium critical dynamics of a non-conserved complex order parameter field. Specifically, we have addressed the situation where the system experiences a sudden change in its parameters that quenches it from a random initial configuration into the critical regime. We have mainly focused on the initial-slip critical exponent θ which governs the universal short-time behavior during the transient non-equilibrium relaxation period before the asymptotic long-time stationary regime is reached. We have employed the perturbative field-theoretical renormalization group method to calculate the value of θ to first order in the dimensional ϵ expansion. Our explicit result turns out identical to that for the equilibrium dynamical model A [12]. Quantum coherence effects do not modify this universal scaling exponent owing to the temporal locality of the one-loop Feynman diagram, or equivalently the fact that the phase term in the correlation propagator is annihilated rendering the results identical to those for the equilibrium system without drive. Rather than analytically calculating the complicated higher-order loop corrections, we have invoked the one-loop renormalization group flow equations [5] as well as a suitable spherical model extension, constructed along the lines of Ref. [70], to argue that the above conclusion likely remains true to all orders in the perturbation expansion.

In the future, we intend to study this and related stochastic dynamical systems by means of direct numerical integration. Comparing the resulting data with our analytical theory should further aid our quantitative understanding of the dynamical critical properties of driven-dissipative quantum systems that experience parameter quenches, and hence take us another step closer towards the ultimate goal of obtaining a complete and systematic classification of non-equilibrium dynamical criticality.

Appendix. Dimensional regularization, Feynman parametrization

In order to arrive at a small expansion parameter for the perturbational analysis in our field-theoretic RG approach, we need to consider non-integer spatial dimensions close and below the upper critical dimension $d_c = 4$. We may consider these non-integer dimensionalities as an analytical continuation of integer ones by means of dimensional regularization. The fluctuation loop integrals in momentum space associated with the Feynman diagrams are tpyically of the following form (see, e.g., Ref. [6]):

$$I_d^{(\sigma,s)}(\tau) = \int \frac{d^dk}{(2\pi)^d} \frac{k^{2\sigma}}{(\tau + k^2)^s} = \frac{\Gamma(\sigma + d/2)\Gamma(s - \sigma - d/2)}{2^d \pi^{d/2} \Gamma(d/2)\Gamma(s)} \, \tau^{\sigma - s + d/2} \; . \tag{2.49}$$

Integrals with different denominators can be reduced to this form through Feynman's parametrization:

$$\frac{1}{A^r B^s} = \frac{\Gamma(r+s)}{\Gamma(r)\Gamma(s)} \int_0^1 \frac{x^{r-1}(1-x)^{s-1}}{[xA + (1-x)B]^{r+s}} \, dx \; . \tag{2.50}$$

These expressions are widely used to evaluate the momentum loop integrals. Euler's gamma function provides the appropriate interpolation for non-integer dimensions.

Chapter 3

Aging phenomena in the two-dimensional complex Ginzburg-Landau equation

3.1 Introduction

Systems can be brought out of equilibrium states through a rapid change of their thermodynamic control parameter(s). If strong fluctuation effects are subsequently generated and govern the relaxation processes, they cannot rapidly return to the stationary states, especially in the continuous transition case or at the critical point where the typical relaxation time scales diverge. “Aging phenomena,” which describe the change of materials properties over time with or without an applied external force, will emerge when this significant slowing-down present [16]. These phenomena are important in physics studies since they provide the probabilities to predict long-time behavior according to the thermal history of associated systems. In these systems time-translation-invariance is spontaneously broken due to the fact that a specified time is chosen to kick the systems out of its equilibrium state, which is usually at $t = 0.0$. Concurrently, a dynamical scaling is also suggested underlying this slow relaxation processes. Thus, a general definition of aging phenomena is given as: physical aging can be observed in a many-body system when its relaxation process satisfies three properties [16]: the relaxation process is slow, i. e. non-exponential relaxation; the breaking of time-translation-invariance; and dynamical scaling is observed. Furthermore, another unexpected property of aging phenomena is that physical aging is also thermoreversible even though the time-translation-invariance is broken, which enhances the importance as better understanding these phenomena.

Two-time quantities are often employed to characterize aging phenomena. For example, the two-time autocorrelation function

$$C(t, s) = \langle \phi(t)\phi(s) \rangle. \tag{3.1}$$

Here $\phi(t)$ generally is the time-dependent order parameter. t is the observation time, and s is called waiting time, which must be earlier than t due to causality. To ensure the emergence of dynamical scaling, we require $t \gg s \gg t_0$, where t_0 referred to as any microscopic time scale. We may expect $C(t, s)$ to follow a simple aging scaling form if aging phenomena is observed:

$$C(t, s) = s^{-b} f_C(t/s), \tag{3.2}$$

where b is the aging exponent and $f_C(y)$ is the scaling function which only depends on the ratio $y = t/s$.

Aging phenomena[16] are known to exist in a broad variety of physical systems, such as Ising model [74, 75], population dynamics models [65], and systems of skyrmions [76]. However, most of the examples we mentioned here are investigating these phenomena using Monte

Carlo simulations or molecular dynamics simulations. A numerical exploration of this topic in fieldtheoretic regime is important to better understand these systems.

To fulfill this objective, we study the complex Ginzburg-Landau (CGL) equation in this paper. The CGL is one of the most studied nonlinear partial differential equations in the physics community. It is thought to be at least a natural description of the kernel of many physical systems that can be characterized by an amplitude (or "envelope" or "modulational") equation. It includes only a simplest cubic nonlinear term; however, it describes a large number of phenomena, spread from nonlinear waves to second-order phase transitions to Bose-Einstein condensation to liquid crystals.

According to the vast library of previous work, a reduced form of the original CGL equation can be obtained through rescaling, and is usually employed in the relevant numerical study. It is

$$\begin{aligned}\partial_t A(\boldsymbol{x},t) &= A(\boldsymbol{x},t) + (1+i\alpha)\nabla^2 A(\boldsymbol{x},t) \\ &\quad -(1+i\beta)|A(\boldsymbol{x},t)|^2 A(\boldsymbol{x},t). \qquad (3.3)\end{aligned}$$

Here, the $A(\boldsymbol{x},t)$ is a complex field, while α and β are two real parameters characterize the linear and non-linear dispersion, respectively. Eq. (3.3) is an amplitude equation of Hopf bifurcation in the spatially homogeneous case. In the spatially extended case, especially in two dimensions, it will express rich behaviors, including spatio-temporal chaos[77], nucleation of spiral wave structures [78] and dynamic freezing [79]. Therefore, it is reasonable to expect aging phenomena to take place in this kind of system. Chaté and Manneville have pointed out that it is promising to investigate aging in the frozen state of two-dimensional CGL[80]; however, there are actually various problems in the observation of aging behavior in most of the states of two-dimensional CGL systems, which we will discuss in details.

3.2 Model description

First of all, in two-dimensional CGL, the strongly fluctuating turbulent states, either with or without topological defects, are hopeless for observing aging, as they are both strong disordering states. Topological defects, specify in two dimensions, are identified by the zeros of the complex field $A(\boldsymbol{x}, t)$. At these points there is singularity of the phase $\theta = argA(\boldsymbol{x}, t)$, since they can not be defined in the case of zero amplitude. The so-called topological charge $n = 1/(2\pi) \oint_C d\theta$ is used to quantify this singularities, where C is a contour around the zero of $A(\boldsymbol{x}, t)$. Only single-charge defects, with $n = \pm 1$, are topologically stable. They can emit stable and well-established spiral waves, which will fill the whole space and make the systems frozen. The relaxation processes of these frozen states, on another hand, is too fast for aging phenomena to be found, which we numerically verify.

However, there is a connection between CGL systems and aging phenomena. It is reported that there aging has been observed in two-dimensional XY models[81]. Indeed, in the special case of $\alpha = \beta = 0.0$, Eq. (3.3) can be reduced to the "real" Ginzburg-Landau (RGL) equation, which describes kinetics resembling the model E for a nonconserved two component order parameter field, namely, the classical two-dimensional XY model[5]. Dynamics of the defects, which actually become vortices, in the real Ginzburg-Landau systems are analogous to charge point. Two oppositely charged topological defects will accelerate towards each other and eventually the attraction will lead to the annihilation of both defects. Similar dynamics should be expected for the CGL case. However, in the frozen state, the surviving topological defects can not interact with each other due to the fact that there are shock structures between different well-established spiral domains. Information is then screened by these shocks and hence no interaction exists between defects in different domains. Therefore, to ensure further slow dynamics, one should try to further destroy these shocks. Das[79] had proposed to introduce disorder in either the α or β parameters to unlock the frozen dynamics. However, this strategy will result in more complicated behavior for the characteristic length of the CGL system. It divides into two significant different sections, the first one corresponds to the transient freezing stage, and the second part is suggested to be consistent with exponential behavior. Thus this strategy actually fails to provide us aging behavior. An interesting fact we notice is that in the previous study from the same group[82] , power law behavior of the characteristic length evolution was observed when one fixed $\alpha = 0.0$ and set $\beta = 0.25$ or 0.5. Aging phenomena can be expected at these points. According to their own suggestion, this is due to the fact that the average length scale $L(t)$ of a single spiral structure is comparable to the wavelength of the associated asymptotic plane wave solution of those spiral waves. Spirals will then behave similarly to those vortices seen in the XY model. This condition will be satisfied either when approaching the "real" Ginzburg-Landau limit in the "focusing-quadrants" where $\alpha\beta < 0.0$ and the spirals are focusing, or when a system is quenched into the "defocusing-quadrant" where $\alpha\beta > 0.0$, and the spiral wave are defocusing. Bohr et al.[11] study the spiral-domain patterns and shocks structures, and also suggest that if the length scale of a single spiral structure is not much larger than the characteristic wavelength, the phase matching constraint may be broken down and no well-established shock lines will be formed.

We study the aging behavior of the two-dimensional complex Ginzburg-Landau equation for both cases respectively, which are distinguished by the winding behavior of related spirals. We extract the dynamic exponent z, which indicates the scaling behavior as $L(t) \sim t^{1/z}$ as well as the corresponding aging exponents of aging phenomena for all the parameter choices we tested. We also try to calculate the autocorrelation exponent λ_C from the scaling function $f_c(y) \sim y^{-\lambda_C/z}$ for the "focusing" spiral case. We do not repeat this step for the "defocusing" case as there is observable bending in the resulting curves for scaled two-time autocorrelations. We claim that our estimate of λ_C may not be very reliable. However, as systems are approaching the XY model for this case, this exponent will provide us probabilities for further comparison of these two models.

3.3 Numerical scheme

We employ standard Euler discretization method to solve Eq. (3.3), with a forward finite differential for time and a central differential for the ∇^2. We will focus on systems on two-dimensional square lattices with periodic boundary conditions. Our system size will be 512×512 and the grid sizes are $\Delta x = 1,\ \Delta t = 0.002$, unless otherwise mentioned. However, we have also tested other system sizes and the $\Delta t = 0.001$ case, which will provide us consistent results here. We will always use entirely random initial configurations to ensuring that we have enough topological defects at the very beginning. We also add a small Gaussian, white, and Markovian noise term $\lambda\eta(\boldsymbol{x}, t)$ into Eq. (3.3) to make it Langevin like. $\lambda = 0.1$ is the noise strength and $\eta(\boldsymbol{x}, t)$ can be characterized by these correlators:

$$\begin{aligned}
\langle\eta(\boldsymbol{x}, t)\rangle &= \langle\eta^*(\boldsymbol{x}, t)\rangle = 0, \\
\langle\eta^*(\boldsymbol{x}, t)\eta(\boldsymbol{x'}, t')\rangle &= \gamma^2\delta(\boldsymbol{x} - \boldsymbol{x'})\delta(t - t'), \\
\langle\eta(\boldsymbol{x}, t)\eta(\boldsymbol{x'}, t')\rangle &= \langle\eta^*(\boldsymbol{x}, t)\eta^*(\boldsymbol{x'}, t')\rangle = 0,
\end{aligned} \tag{3.4}$$

with $\gamma = 0.2$ and $\eta^*(\boldsymbol{x}, t)$ as the complex conjugate of $\eta(\boldsymbol{x}, t)$.

The characteristic length of system is thought to be the average size of spiral domains and can be calculated as:

$$l(t) = \frac{L}{\sqrt{N(t)}}. \tag{3.5}$$

Here $L = 512$ is the linear size of our system and $N(t)$ is the total number of topological defects in the system at time t. To investigate the aging phenomena, we also need to calculate

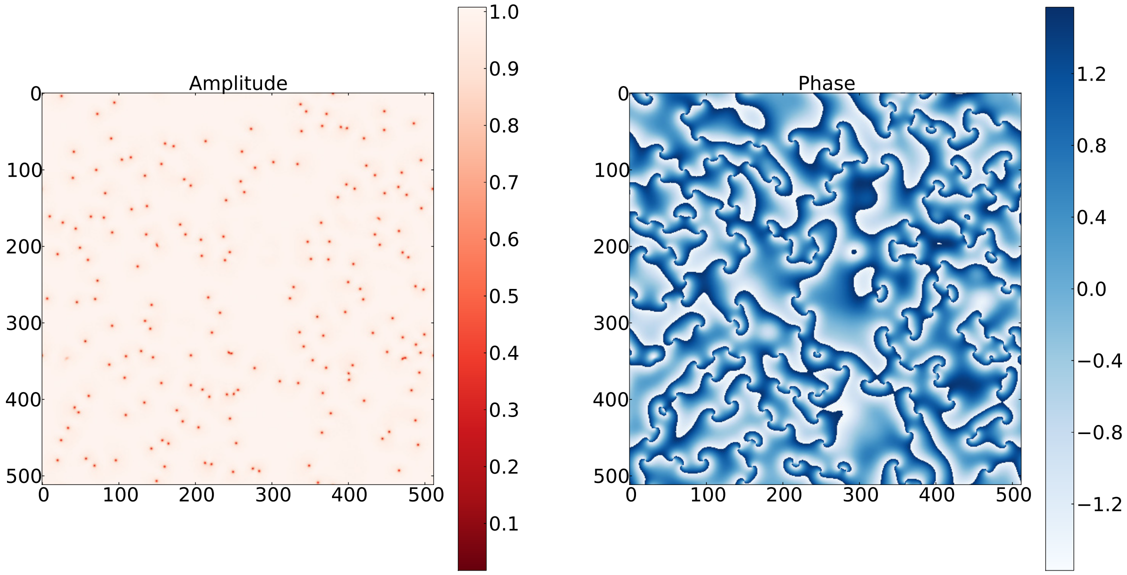

Figure 3.1: An example system configuration obtained from the solution of CGL on a two-dimensional square lattice for the focusing spiral wave case when quenched near the RGL limit with $\alpha = -0.05$; $\beta = 0.5$ and $t = 500$. The white-red plot (on the left) shows the amplitude of the complex order parameter; the blue-white one depicts the phase.

the two time autocorrelation function. However, since we are working with complex order parameter, we need to modify Eq. (3.1). We will estimate the modulus of this complex function as follow:

$$C(t,s) = |\langle A(\boldsymbol{x},t)A^*(\boldsymbol{x},s)\rangle|. \tag{3.6}$$

$A^*(\boldsymbol{x},t)$ is the complex conjugate of $A(\boldsymbol{x},t)$. Without ambiguity, this is what we refer to as the two-time autocorrelation function in rest of this letter.

3.4 Results

We consider both the focusing spiral wave case when systems are quenched near the RGL limit and the defocusing spiral wave case. Fig. 3.1 shows example plots of system configurations for the focusing case. In the phase plot (blue-while one, or right one), there are small spiral structures which are not well-established due to the fact their wavelength is comparable to their average size, and hence there will be no significant shock structures in the amplitude plot (red-white one, or left one). Most of the space in the amplitude plot holds an amplitude around $|A(\boldsymbol{x}, t)| = 1.0$ except for those deep red points which are topological defects cores with zero amplitude. There is no spontaneous creation of defect pairs in this case. They just try to approach the nearest neighbor with opposite topological charge and annihilate with each other. Due to this, there are spiral waves in the phase plot. When the distance between two oppositely charged defects are close enough, instead of directly approaching like vortices in the XY model, they tend to drift along the tangential direction, and merge gradually and eventually annihilate. Some residual of the shocks can be viewed in the amplitude plot as the bright still regions that indicate $|A(\boldsymbol{x}, t)| > 1.0$. These residual, will become prominent when departing from the RGL limit and will finally partition systems into clearly separated domains. The dynamics will become freezing in this case. Defects with defocusing spiral will behave similarly to the focusing case, except the spirals rotate differently.

As shown in Fig. 3.2 (a), there is suggestive scaling behavior of the characteristic length of the CGL system with control parameter pair $(\alpha, \beta) = (-0.05, 0.5)$ if the strong fluctuating part due to the finite size effect is ignored. A dynamic exponent $1/z = 0.307$ can be extracted. It is relatively smaller than the value $1/z = 0.5$, which is obtained in the two-dimensional XY model below the critical temperature and quenched from a totally disordered initial state[74]. A logarithmic correction in the relation between the characteristic length and the time, $l(t) \sim (t/\ln t)^{1/z}$ is also acquired in the latter case. However, if we also apply this logarithmic correction in our CGL case, the resulted scaling behavior of the characteristic length is even worse than the no correction case with an aging exponent $b \sim 0.8$ and the autocorrelation exponent $\lambda_C/z = 1.49$. Again compared with the XY model [81] where $b = 0.03$ and $\lambda_C/z = 1.05$ when $T/T_c = 0.3$, both our aging exponent b and auto-correlation

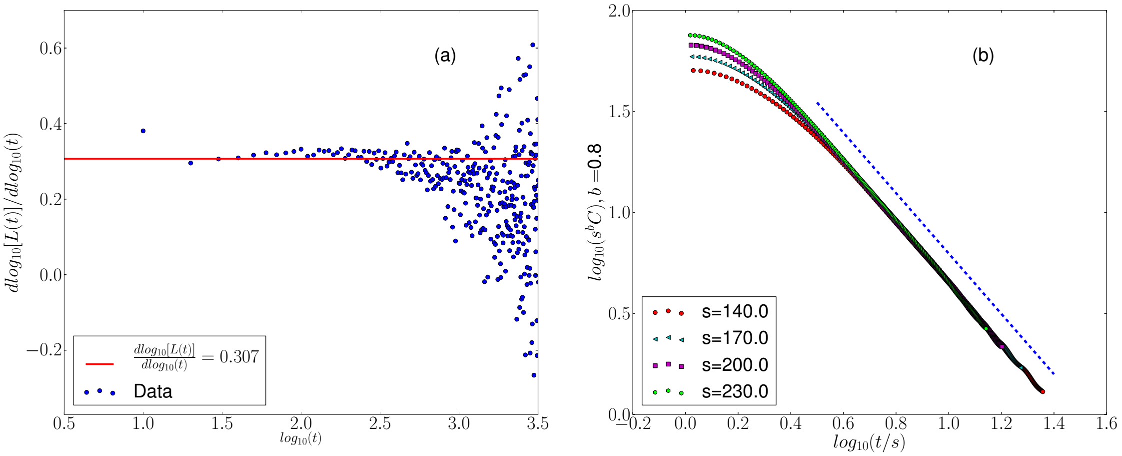

Figure 3.2: (a) The derivative of the logarithm of the characteristic length of the two-dimensional CGL system with respect to the logarithm of the time, with control parameters $\alpha = -0.05$; $\beta = 0.5$, namely for focusing spirals. (b) the scaled two-time autocorrelation function for various waiting time s. The aging exponent here is $b = 0.8$. The blue dashed line with slope 1.49 is roughly parallel to the collapsed curve, which indicates the autocorrelation exponent $\lambda_C/z = -1.49$. The data result from averaging over 1000 independent runs.

exponent λ_C are larger. All these facts suggest that the scaling and aging behavior of the CGL systems with nonvanishing control parameter pair (b, c) is clearly different from the classic XY model. We then try to vary the control parameter pair (b, c) to reinforce our conclusions. Relevant results are listed in Table 3.1. We use 1000 independent realizations for each parameter pairs. We only try to extract the autocorrelation exponent when we think we see a meaningful value, namely when the scaled autocorrelation function looks linear.

Table 3.1: Measured values of the dynamic, aging scaling, and autocorrelation exponents for the focusing spiral case

(α, β)	$1/z$	b	λ_C/z
$(-0.05, 0.5)$	0.307 ± 0.003	$[0.69, 0.80]$	1.49 ± 0.02
$(-0.05, 0.4)$	0.354 ± 0.003	N/A	N/A
$(-0.05, 0.6)$	0.293 ± 0.004	$[0.35, 0.44]$	1.22 ± 0.01
$(-0.04, 0.5)$	0.312 ± 0.003	$[0.72, 0.85]$	1.42 ± 0.02
$(-0.06, 0.5)$	0.298 ± 0.004	$[0.63, 0.77]$	1.45 ± 0.01

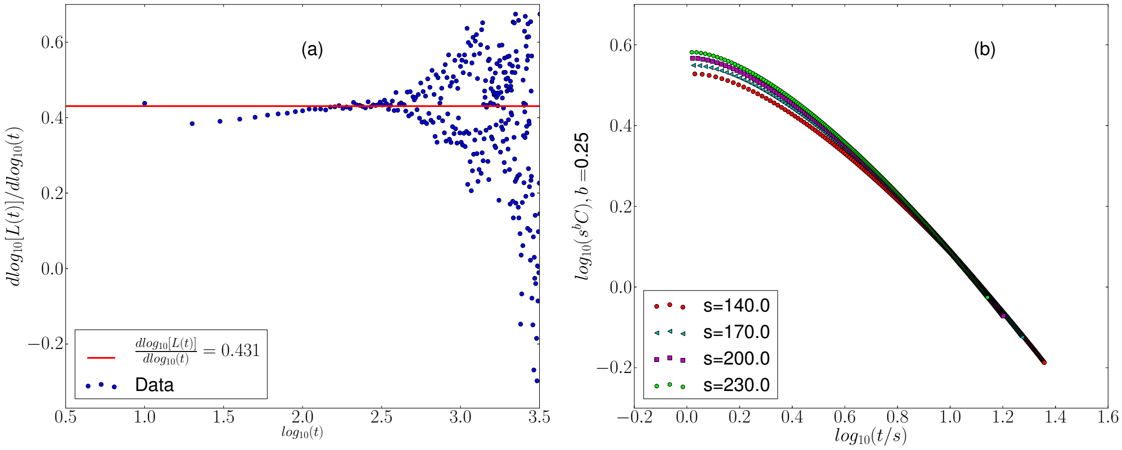

Figure 3.3: (a) The derivative of the logarithm of the characteristic length of the two-dimensional CGL system with respect to the logarithm of the time, with control parameters $\alpha = 1.176$; $\beta = 0.7$, namely for defocusing spirals. (b) the scaled two-time autocorrelation function for various waiting times s. The aging exponent here is $b = 0.25$. These results were obtained by averaging over 8000 independent runs.

Here we focused ourselves the small α case, as it can be directly related to the spatial scale. According to the extracted values of the aging exponent b, we conclude that these suggest a non-universal behavior of our CGL systems with focusing spirals. This is reasonable since the non-vanishing linear term in Eq. (3.3) automatically assumes that we are below the critical point here. The variance is stronger when we change the parameter β in this small α case, while only slightly changing if we change α. This is because β contributes much more than α to the deviation from the RGL limit $\alpha = \beta = 0.0$. Furthermore, the $(-0.05, 0.6)$ systems become almost frozen at the very end. The scaled two-time autocorrelation functions curves are observed to be dispersed in this parameter choice. On the other hand, the $(-0.05, 0.4)$ systems show no significant aging scaling behavior during the time regime we observe. This absence of aging phenomena can be viewed as more evidence of non-universal behavior.

Aside from the small α case in the focusing spiral quadrant, which is considered to explicitly approach the RGL limit, one can also eliminate the significant shock structures and have interactive spiral dynamics through quenching the systems into the defocusing quadrant,

Table 3.2: Measured values of the dynamic, and aging scaling exponents for the defocusing spiral case

(α, β)	$1/z$	b
$(1.176, 0.7)$	0.410 ± 0.003	$[0.13, 0.25]$
$(1.176, 0.65)$	0.406 ± 0.003	$[0.20, 0.26]$
$(1.176, 0.55)$	0.394 ± 0.003	N/A
$(1.111, 0.6)$	0.416 ± 0.003	$[0.20, 0.28]$
$(1.429, 0.55)$	0.388 ± 0.003	N/A
$(1.429, 0.6)$	0.394 ± 0.003	N/A
$(1.250, 0.55)$	0.392 ± 0.003	N/A
$(1.250, 0.6)$	0.399 ± 0.003	N/A

where $\alpha\beta > 0.0$. In this case, it is not necessary to set the control parameters near the origin in the $\alpha - \beta$ parameter space. An example plot which shows the dynamic exponent z is displayed in Fig. 3.3 (a). The value $1/z = 0.431$ is clearly different from the focusing spiral quadrant, which is indicative of different dynamic behaviors for those two cases. The associated scaled two-time autocorrelation functions are also shown in Fig. 3.3 (b). First of all, we see that there is obvious bending even in the collapsing section of those curves. This means the simple form of the scaling function $f_c(y) \sim y^{-\lambda_C/z}$ is broken. Therefore, it is unreasonable to still extract the autocorrelation exponent λ_C, so we will merely consider the dynamic and aging exponents in this case.

In Table 3.2 we show our overall results for different parameter pairs. Except for the $(1.176, 0.7)$ pair, other results are obtained through averaging over 1000 independent realizations. The dynamics exponents z are generally smaller and show little change across different parameter pairs, compared with the focusing cases. In the aging scaling case, the measured credible ranges of aging exponents b do have overlaps. However, due to the fact that aging phenomena are not significant for 5 parameter pairs (where we put a "N/A" sign for the aging exponent) we want to make our conclusion about the universality of this exponent more carefully. To this end, we want to first answer the question of why dynamical scaling behavior can generally exist and why spirals can behave like vortices even in systems that are quenched far from the RGL limit $\alpha = \beta = 0$. In fact, there exists a more general case for Eq. (3.3) other than the RGL limit, which is obtained by setting $\alpha = \beta \neq 0$. This special case can be related to the RGL limit through a transformation into a "rotating" frame $A \to A\exp(ibt)$ if one is going to obtain an approximately analytic solution of Eq. (3.3) for the isolated spiral case[7]. After neglecting high-order corrections, the resulting solution is identical with the RGL solution except for a shift in the wavenumber. In other words, there exists a whole branch of vortices-like behavior limit in the defocusing quadrant, which is not the case when $\alpha\beta < 0.0$. Systems that are quenched far from the origin in $(\alpha - \beta)$ parameter space in defocusing quadrant can still show nice dynamical scaling and aging when their control parameter pair is set near the line $\alpha = \beta$. This fact, as well as our numerical results in Table 3.2, suggest that the criterion for significant aging phenomena emerging or not is that aging scaling is restored when the control parameter pairs approaching the limit $\alpha - \beta \to 0$. The asymptotic wavenumber of the spiral vanishes in this limit. Therefore, the effect of shock structures is assumed to be weak here. However, due to the fact that when $\alpha = \beta \neq 0$ there is still an obvious rotation of the equiphase lines, the interaction between defects is expected to be oblique repulsion and attraction. Two defects will never approach each along the line connecting them, like the vortices in RGL case. They will either spiral with respect to each other if they are like-charged, or move along the tangential direction, or approach each gradually and finally annihilate with each other in the oppositely charged case.

We then further test this criterion by explicitly quenching the control parameter near the $\alpha = \beta$ limit and shows our results in Table 3.3.

Firstly, the result of aging exponent $b = 0.03$ from previous study of the two-dimensional

Table 3.3: Measured values of the dynamic and aging scaling exponents for the defocusing spiral case, near the limit $\alpha = \beta$

(α, β)	$1/z$	b
$(1.2, 1.2)$	0.441 ± 0.002	$[0.00, 0.13]$
$(1.0, 1.0)$	0.426 ± 0.003	$[0.00, 0.13]$
$(1.2, 1.25)$	0.444 ± 0.002	$[0.00, 0.15]$
$(1.2, 1.15)$	0.440 ± 0.003	$[0.00, 0.13]$

XY model below the critical temperature[81] falls into all the extracted credible ranges of b in these tests. This confirm the analytic conclusion that CGL will restore some XY model behaviors when approaching the $\alpha = \beta \neq 0$. The dynamical scaling exponent z is also observed to be closer to the limit $1/z = 0.5$ than that in Table 3.1 and Table 3.2. The remaining deviation can be either from the fact that CGL still holds different dynamical scaling behavior from the XY model, or from the logarithmic correction issue. Further studies are needed to confirm these effects. And finally, although these aging exponents share similar ranges in Table 3.3, they are clearly different from those in Table 3.2, which will also suggest a non-universal behavior of the spirals in the defocusing quadrant. Aside from that, the slightly bending features persist even if we are in the limit case $\alpha = \beta$. We may tentatively suggest that this is because the equiphase lines of the resulted spirals (or vortices) are defocusing rotating, which will definitely affect the dynamics of those spirals.

3.5 Conclusion

In summary, we have investigated the dynamic scaling and aging phenomena in the two-dimensional CGL equation, both in the focusing and defocusing spiral quadrants. To avoid the shock structures which will prevent the interaction between defects and cause the systems to become frozen, we should quench the control parameters near the RGL limit $\alpha = \beta = 0.0$

in the focusing spiral case or be in the defocusing quadrant. In the time regime we considered here, both the dynamical scaling and aging are slightly different from the vortices behavior in the two-dimensional XY model when quenched below the critical temperature in the focusing spiral systems, even if they are considered to be approaching to that limit. In fact, the aging phenomena will even turn out to be absent for some control parameter pairs, serving as evidence that there exist non-universal scaling behavior in these systems. In the defocusing spiral case, as one can approach another limit case $\alpha = \beta$ while not having to be near the regime of $\alpha = \beta = 0$, aging phenomena can still be restored even if systems are quenched far away from the origin in the parameter space. This non-universal behavior is suggested again by our observations. A slightly bending of the scaled two-time autocorrelation function curves is always found in all the defocusing spiral cases, whether the aging scaling behaviour emerges or not. We tentatively assumed that this can be viewed as an effect of the defocusing rotation of the equiphase lines connecting different topological defects(or vortices). Thus, no simple aging scaling exists in this defocusing spiral quadrant. Better statistical data, as well as larger system sizes, are needed to further confirm those conclusions. Different boundary conditions, and other initial configurations, e. g. uniform initial configurations with slight perturbations may also be important here since the scaling behavior of these systems is non-universal.

Chapter 4

Nucleation of spatio-temporal structures from defect turbulence in the two-dimensional complex Ginzburg–Landau equation

4.1 Introduction

Spontaneous spatial structure formation, as well as its inverse process, the dynamical destruction of patterns through spatio-temporal chaos, are of considerable interest, especially in far-from-equilibrium systems. These phenomena are encountered in condensed matter physics, chemistry, and biology. Studies of this topic have benefited from the recent development of careful experiments, as well as analytic and numerical tools. Non-equilibrium spatial patterns often emerge due to linear system instabilities that are induced by varying some control parameter(s) beyond certain thresholds [50, 51]. The term "ideal pattern" is defined to represent the spatially periodic structure of an infinitely extended system. Defects, which can generally be viewed as any departure from this ideal pattern, constitute important "real pattern" effects. Their structures may reflect the topological characteristics of the ideal patterns in a (quasi-)stationary dynamical state. For example, the stationary kinetics in non-equilibrium steady states as well as the relaxation towards such stationary regimes are often governed by the properties of topological defects in these non-linear dynamical systems. Indeed, the onset of spatio-temporal chaos in excitable or oscillatory media can trigger the appearance of topological defects, which are point-like objects in two dimensions, but can be extended in higher dimensions. A striking example are the famous chemical oscillations in the Belousov–Zhabotinsky (BZ) reactions [83–87], where the defect points emit spiral chemical waves. Such striking wave patterns are also observed in spatially extended stochastic population dynamics, e.g., the stochastic May–Leonard model with three cyclically competing species [88–91]. Other types of topological defects are encountered in driven systems maintaining non-linear traveling waves such as Rayleigh–Bénard convection in planar nematic liquid crystals [92, 93], or electroconvecting nematic liquid crystals [94]. Here the defects constitute dislocations in the roll pattern of the traveling waves [95].

A simple, generic description of many pattern-forming systems is afforded through the complex Ginzburg–Landau equation (CGL). Indeed, the CGL is considered to at least represent the "kernel" of many amplitude equation models [80] that have been employed to characterize spontaneous spatial pattern formation [95, 96]. A large number of numerical studies of the CGL in two dimensions has been performed over the past three decades, and uncovered a wide variety of intriguing dynamical behavior upon varying certain control parameters. In this work, we mostly consider the transition from the "defect-mediated turbulence" state with strong spatio-temporal fluctuations to the so-called "frozen" state displaying beautiful stationary spiral wave patterns that resemble structures observed in two-dimensional oscillating media (e.g., the BZ reactions and the stochastic May–Leonard model). Only a few previous studies have addressed the transition dynamics between these two states, namely the crossover from the strongly fluctuating into a dynamically frozen state [78]. This process is thought to be important for controlling spatio-temporal chaos in spatially extended systems [97, 98]. The inverse transition has been also observed in a real BZ reaction with an open reactor [99]. The transition between turbulent and frozen spiral states can be altered by adding a chiral symmetry breaking term into the right-hand-side of the CGL [100], which also modifies the specific form of the dynamical equation and hence the phase diagram. To obtain a better understanding of the accompanying transient processes, we aim for a quantitative characterization of the transition dynamics, where one switches the control parameters beyond a transition limit in parameter space. The defect-mediated turbulence state is thus rendered meta-stable, and well-established spiral structures emerge. As pointed out in Ref. [78], when turbulence becomes transient, the onset of the formation of spiral wave structures can be viewed as a nucleation process. The authors of Ref. [78] primarily investigated situations where the control parameters were chosen near the crossover regime, and hence the defect-mediated turbulence state becomes just unstable. In the present study, we conversely also consider sudden parameter switches which represent deep quenches into the stable frozen state regime. Based on our numerical results and subsequent finite-size extrapolation analysis, we obtain evidence for a non-vanishing nucleation barrier for the formation of spiral structures. Consequently we conclude that the transition from the defect turbulence to the quasi-stationary frozen state is of a discontinuous nature.

In addition to spiral wave structures, reaction-diffusion systems may also exhibit “target wave patterns” in the presence of spatial inhomogeneities. For example, the BZ reaction supports target waves if a dust grain or other impurity is inserted [83, 85]. According to Refs. [101, 102], a pacemaker is needed to stabilize the resulting wave pattern. However, target patterns can also emerge in a homogeneous system if it is subjected to perturbations with oscillating concentrations [101–104]. The singularity point in the defect center will assume this trigger role for stable spiral structures, whence spontaneous creation and annihilation of defect pairs may occur. Those pacemakers or nucleation centers ensure that the internal regions of those heterogeneous nuclei will maintain an effectively higher oscillation frequency than the outside bulk of the oscillatory medium, which is the reason why a local inhomogeneity is needed to generate target waves. However, in contrast to rotating spirals, target waves take a concentric circular shape, and propagate radially outward from their source. Previous work indicated that target waves are characterized by a vanishing topological charge [105], in distinction to the positively or negatively charged (oriented) spirals. There are also intriguing studies of spatiotemporal chaos control through target waves [106]. Thus, in this work we also study target wave nucleation and compare this scenario with the aforementioned spiral droplet nucleation.

This paper is structured as follows: A general review of the CGL model is presented in section 4.2; section 4.3 describes our numerical scheme as well as the methodology we devised to characterize the spatial scale of the CGL system, especially when it contains “droplet” nucleating structures, and to determine the nucleation time distribution. In section 4.4, we implement our algorithm and numerical analysis to study spontaneous spiral droplet nucleation events in two-dimensional CGL systems subject to two distinct quench protocols: namely either from fully randomized initial conditions, or from initial configurations that correspond to stationary states in the defect turbulence region. Target wave nucleation with an artificially prepared pacemaker are investigated and analyzed in section 4.5. Finally, we summarize our results in the concluding section 4.6.

4.2 Model Description

A general description of non-linear driven-dissipative systems is afforded by the complex Ginzburg–Landau equation in terms of a complex field $A(\boldsymbol{x}, t)$ [107–109]. $A(\boldsymbol{x}, t)$ provides the amplitude and phase of the lowest Fourier mode of a characteristic quantity $C(\boldsymbol{x}, t)$ describing the system. Therefore, $C(\boldsymbol{x}, t)$ can be decomposed as:

$$C(\boldsymbol{x}, t) = C_0 + A(\boldsymbol{x}, t)e^{i\omega_0 t} + c.c. + h.o.t., \tag{4.1}$$

where C_0 is a constant, *c.c.* means complex conjugation, and *h.o.t.* denotes higher-order terms. Furthermore, compared with the frequency scale ω_0, the complex field $A(\boldsymbol{x}, t)$ is assumed to be slowly varying. $A(\boldsymbol{x}, t)$ is often called order parameter, and obeys the CGL which can be written in a rescaled form:

$$\begin{aligned} \partial_t A(\boldsymbol{x}, t) &= A(\boldsymbol{x}, t) + (1 + ib)\nabla^2 A(\boldsymbol{x}, t) \\ &\quad -(1 + ic)|A(\boldsymbol{x}, t)|^2 A(\boldsymbol{x}, t), \end{aligned} \tag{4.2}$$

with real constants b and c that characterize the linear and non-linear dispersion, respectively. Here, the parameters that describe the deviation from the transition threshold, the diffusivity, and the non-linear saturation have been rescaled to 1. Note that the frequency shift (the imaginary part of the coefficient of the linear term) is eliminated by gauge symmetry. Eq. (4.2) is invariant under the transformation $(A, b, c) \to (A^*, -b, -c)$ [7]. Therefore, we only need to consider half of the parameter space in the b-c plane and can directly predict same behavior of the system from this mapping; for example, in the two-dimensional (b, c) parameter space, the first and third quadrants are equivalent due to that invariance transformation. The first and third quadrants are labeled "defocusing quadrants", since the associated spiral waves rotate along the same direction as the equi-phase lines (or spiral arms). The second and fourth quadrants are correspondingly called “focusing quadrants”, and yield spirals that rotate inversely with respect to the defocusing quadrants. We shall restrict ourselves to the focusing case in this paper.

The CGL (4.2) describes spatially extended systems whose homogeneous state is oscillatory around the threshold of a super-critical Hopf bifurcation, e.g., for which the stable stationary dynamical state becomes a global limit cycle. The isotropic non-linear partial differential equation (4.2) reduces to the “real” Ginzburg-Landau Equation (GL) for $b = c = 0$. It may also be viewed as a disspative extension of the conservative non-linear Schrödinger equation [7], which formally follows in the limits $b, c \to \infty$ in Eq. (4.2).

There exists a simple homogeneous solution of Eq. (4.2), namely $A = \exp(-ict + \phi)$ with frequency $\omega = c$ and an arbitrary constant phase ϕ. This spatially uniform periodic solution becomes unstable when $1 + bc < 0$, known as the Benjamin–Feir limit. Long-wavelength modes with wave numbers below a critical threshold proportional to $\sqrt{|1 + bc|}$ will then be exponentially enhanced. A more general solution form is a family of traveling plane wave solutions,

$$A(\boldsymbol{x}, t) = \sqrt{1 - Q^2}\, e^{i(\boldsymbol{Q}\cdot\boldsymbol{x} - \omega t)}, \tag{4.3}$$

with frequency $\omega = c + (b - c)Q^2$, restricted to $Q^2 < 1$. The homogeneous oscillating solution is restored in the limit $Q \to 0$. The stability of this solution can be tested through perturbing the plane wave solution (4.3) with modulation modes and studying their complex growth rate [7, 110, 111]. Restricting the analysis to the most dangerous longitudinal perturbation and performing a long-wavelength expansion (with $b \neq c$ and $Q \neq 0$), one arrives at the Eckhaus criterion for the plane wave solution (4.3) that can be tested against convective instability for non-zero group velocities [112–114], for which the initial localized perturbation will be amplified. However, at fixed position, it can in fact not be amplified due to the drift

[115]. The absolute instability limit is obtained by considering the evolution of a localized perturbation in the linear regime, given by

$$S(\boldsymbol{x},t) = \int \frac{d^d k}{(2\pi)^d} \hat{S}_0(\boldsymbol{k}) e^{i\boldsymbol{k}\cdot\boldsymbol{x}+\lambda(\boldsymbol{k})t}, \tag{4.4}$$

where $\hat{S}_0(\boldsymbol{k})$ denotes the Fourier transform of the initial perturbation $S_0(\boldsymbol{x})$, and $\lambda(\boldsymbol{k})$ represents the growth rate of specific modulational modes with wave vector $\boldsymbol{k}$ [116]. In the asymptotic time limit $t \to \infty$, the integral will be dominated by the largest saddle point of the growth rate $\lambda(\boldsymbol{k})$. The criterion of absolute instability finally is given by

$$\mathrm{Re}[\lambda(\boldsymbol{k}_0)] > 0,\ \partial_{\boldsymbol{k}}\lambda(\boldsymbol{k})|_{\boldsymbol{k}_0} = 0. \tag{4.5}$$

It suggests that the Eckhaus instability is more restrictive than the absolute stability limit when $Q \neq 0$ [111]. “Spatio-temporal” chaos, which has received continuous interest over the past decades, is obtained upon moving beyond those limits into the unstable regime in the $(b-c)$ parameter plane.

In order to specifically describe the dynamics in the phase-unstable regime $1+bc < 0$ and near the bifurcation threshold, one may just consider the most unstable modes [117]; namely, only the phase term constitutes a relevant order parameter when its gradients remain sufficiently small. The emerging “phase turbulence” regime is characterized by relatively weaker spatio-temporal chaos without the presence of topological defects (see below). Manneville and Chaté characterized the statistical properties of this state through evaluating the parameters of an effective Kardar–Parisi–Zhang equation [8]. However, this reduced description breaks down in the limit $1 + bc \ll -1$ [77].

Here, a turbulent state with strong coupling between the amplitude and phase modes emerges, named “amplitude turbulence”, and governed by exponential decays of the correlation function in both time and distance; therefore, no long-range temporal or spatial order persists. The existence of hysteretic behavior observed in Refs. [9, 77, 118] as well as the Lyapunov exponent measured through different methods [119] suggest that the transition from a homogeneous periodic solution to this amplitude turbulence regime is discontinuous. The appearance of the turbulent state is accompanied by the presence of topological defects, which will take the form of points in two spatial dimensions, and defect lines in three dimensions, and are located at the points where $|A(\boldsymbol{x}, t)| = 0$, or the phase gradient of $A(\boldsymbol{x}, t)$ diverges [119]. They can be characterized by the quantized circulation

$$\oint_C d\theta = 2\pi n, \;\; n = \pm 1, \pm 2, \ldots, \tag{4.6}$$

with $\theta = \arg A$, and where C denotes an arbitrary closed path which encloses the core of a defect, and the integer n represents a “topological charge”. Previous studies suggest that multiply charged defects are unstable and will split into a set of single-charged defects [120]. The mechanism of defect creation was described in earlier work as well [77]. In the phase-unstable regime, the phase turbulence quickly saturates, and phase gradients increase rapidly. This will eventually lead to a pinching of the equi-phase, followed by a shock-like event. This sequence hence creates a pair of topological defects with opposite charge [121]. Since in the ultimate well-established turbulent state, the system will tend to have a uniform distribution of topological charge, these creation events are likely to happen “far from” any existing defects, implying a constant defect generation rate. On the other hand, defect pair annihilation processes can be understood on a mean-field level assuming random defect motion. The annihilation rate will then be roughly proportional to the square of the defect number inside the system [78, 122]. Finally, the “defect-mediated turbulence” regime describes a stationary configuration with defects continuously appearing, moving, mixing, and annihilating [77, 117, 122–124]; it is consequently characterized by the balance of spontaneous creation and annihilation of topological defects.

In the special case $b = c$, the dynamics of the system described by Eq. (4.2) will resemble the critical dynamics of "model E" [13] for a non-conserved two-component critical order parameter field, e.g., in a planar ferromagnet or superfluid in equilibrium [6], and restores the "real" GL. In two dimensions, it yields the dynamics of the Berezinskii–Kosterlitz–Thouless transition observable, e.g., in superfluid helium films [125]. The topological defects will take the form of vortices as in the planar XY model; if $b = c \neq 0$, the vortices will rotate. When $b \neq c$, topological defects may emit spiral waves whose arms (the equi-phase lines) behave as those of an Archimedean spiral [87]; they can either propagate inward or outward. Those spiral wave structures are thought to be very important features in biological systems [126]. Stable spiral waves can be formed beyond a certain limit in the b-c plane where the turbulent state becomes metastable. The existence of localized amplitude modes, i.e., stable topological defects, will allow nucleation to happen, and thereby eventually generating stable spiral structures in the system.

Aside from directly varying the control parameters (b, c), one may also change the two-dimensional CGL system behavior by introducing suitable spatially localized inhomogeneities, which will modify Eq. (4.2) by adding a local perturbation on its right-hand-side. This additional heterogeneity can facilitate the formation of so-called "target wave" patterns. Specifically, if the local oscillation frequency in the perturbed spatial patch is set to be lower than in the surrounding bulk, and if the homogeneous solution of Eq. (4.2) has a stable limit cycle, there should be a unique solution independent of the initial condition as $t \to \infty$, which is comprised of radially outward propagating waves that originate from the localized inhomogeneity [127]. Asymptotically, those spreading fronts should behave just like plane waves (4.3). According to Hagan's theoretical study [101], there actually exists a unique and stable heterogeneous target wave solution of the modified CGL (4.2) with an additional inhomogeneity. Its most common form is introduced by setting the control parameters (b, c) within a small region different from its surrounding environment. Furthermore, two different types of target wave solutions, distinguished by an additional superimposed temporal modulation at another frequency in one of them, can be obtained if a more complicated spatial inhomogeneity is introduced in the system [127]. Target wave solutions can also be generated by boundary effects [128].

When wave fronts emitted by different sources, e.g., topological defects or even heterogeneous nuclei, collide, their interaction causes the appearance of a "shock", i.e., in two dimensions a thin linear structure in the modulus field. These shocks are considered to be very strong perturbations marked by a sudden increase of $|A|$. As they can absorb incoming perturbations, interactions between waves originating from different sources become effectively screened. The shocks may be viewed as the boundaries of different domains of spiral or target waves, which consequently generate "droplet" structures in the amplitude landscape for either wave pattern. During the initial growth process of a spatio-temporal pattern, there will also be shocks formed between the corresponding wave and its surrounding turbulent structures. As the droplet sizes increase, those shocks will push the surrounding defect turbulence piedmonts away. As an indirect result, this process accelerates the annihilation of defect pairs with opposite topological charge since the spatial regions governed by defect turbulence are being compressed, and defects with opposite charge are brought into closer vicinity.

During the spiral nucleation process, until the entire space is filled, each spiral structure will occupy a certain domain with a length scale that is usually much larger than the wavelength of the spiral waves. Those domains are separated by shock lines and are typically four- or five-sided polygon-like structures; their boundary shocks are approximately hyperbolic [11, 129]. Defects may also exist in the spiral far-field regime; these are thought to be passive objects that persist inside the shock region, "enslaved" by the vortex of a spiral domain. This CGL (quasi-)stationary state was termed “vortex glass” by Huber et al. [78], and “frozen” state by Chaté et al. [80], since the dynamics in this regime becomes extremely slow; hence this state may persist indefinitely, at least in finite systems [7]. Several studies have aimed at quantitatively analyzing the relaxation processes in the frozen state [130], as well as the “unlocking” of freezing [79, 131, 132]. Aranson et al. [133, 134] investigated the interaction between different spirals in both symmetric and asymmetric situations, as well as the mobility of spirals when driven by external white noise [135, 136]. The competition between spiral and target patterns was studied by Hendrey et al. [127].

In this paper, we are predominantly interested in the incipient stages in the formation of spiral structures or target waves following a sudden quench from a random initial configuration, or alternatively from the defect-turbulent regime, namely nucleation processes, and the ensuing transient kinetics [137].

4.3 Numerical Scheme and Nucleation Measurement

In this paper, we limit ourselves to studying the CGL on a two-dimensional spatial domain with periodic boundary conditions. We implement Eq. (4.2) on a square lattice using the standard Euler discretization, employing central differentials in space and forward finite differential in time. Our discretization mesh sizes were $\Delta x = \Delta y = 1.0$, and $\Delta t = 0.001$. We should clarify the reason for choosing a relatively smaller (by a factor of ten compared to previous studies [78, 132]) differential time step: Since defect turbulence is spontaneously created by intrinsic chaotic fluctuations rather than external noise, the stability of the continuous partial differential equation (4.2), as well as the stability of the numerical solution scheme definitely require careful consideration. This caveat is supported by numerical experiments: The stable regime of temporal periodic solutions and phase turbulence in the $b - c$

parameter plane becomes successively compressed as the individual integration time steps are increased. Consequently, the differential scheme itself is rendered unstable. Therefore, in order to avoid such numerical artifacts and still maintain acceptable computational efficiency, we choose $\Delta t = 0.001$ as a reasonable differential time step for our implementation.

In order to handle the complex field $A(\boldsymbol{x}, t)$, we separate its real and imaginary parts, $A(\boldsymbol{x}, t) = A_r(\boldsymbol{x}, t) + iA_i(\boldsymbol{x}, t)$; Eq. (4.2) thus splits into two coupled real partial differential equations for $A_r(\boldsymbol{x}, t)$ and $A_i(\boldsymbol{x}, t)$ respectively:

$$\begin{aligned} \partial_t A_r &= A_r + \nabla^2 A_r - |A|^2 A_r - b\nabla^2 A_i + c|A|^2 A_i, \\ \partial_t A_i &= A_i + \nabla^2 A_i - |A|^2 A_i + b\nabla^2 A_r - c|A|^2 A_r. \end{aligned} \tag{4.7}$$

The finite differential scheme described above can then be readily applied to numerically solve these two coupled partial differential equations.

To quantitatively characterize the nucleation in CGL systems, a previous study [78] chose to monitor the defect density, or equivalently the number of topological defects $n(t)$ in a fixed domain area L^2 as function of simulation time t. A corresponding typical defect separation length is then given by $l_{\text{sep}}(t) = L/\sqrt{n(t)}$ for a system with linear dimension L. The nucleation time can be measured by determining when the associated defect density drops below, say, two standard deviations from its statistical average in the transient turbulent state. However, as noted in Refs. [122, 124, 138], the number of topological defects fluctuates around a mean value $\bar{n}$ with variance $(\Delta n)^2 = \bar{n}$. Thus, as in typical simulation domains $\bar{n}$ is large in the defect turbulence state, the ensuing sizeable fluctuations will render the resulting nucleation time rather inaccurate.

This is illustrated in Fig. 4.1, where we test two individual systems with different control parameter pairs, namely (a,b): $b = -3.5$, $c = 0.556$, which is close to the transition regime

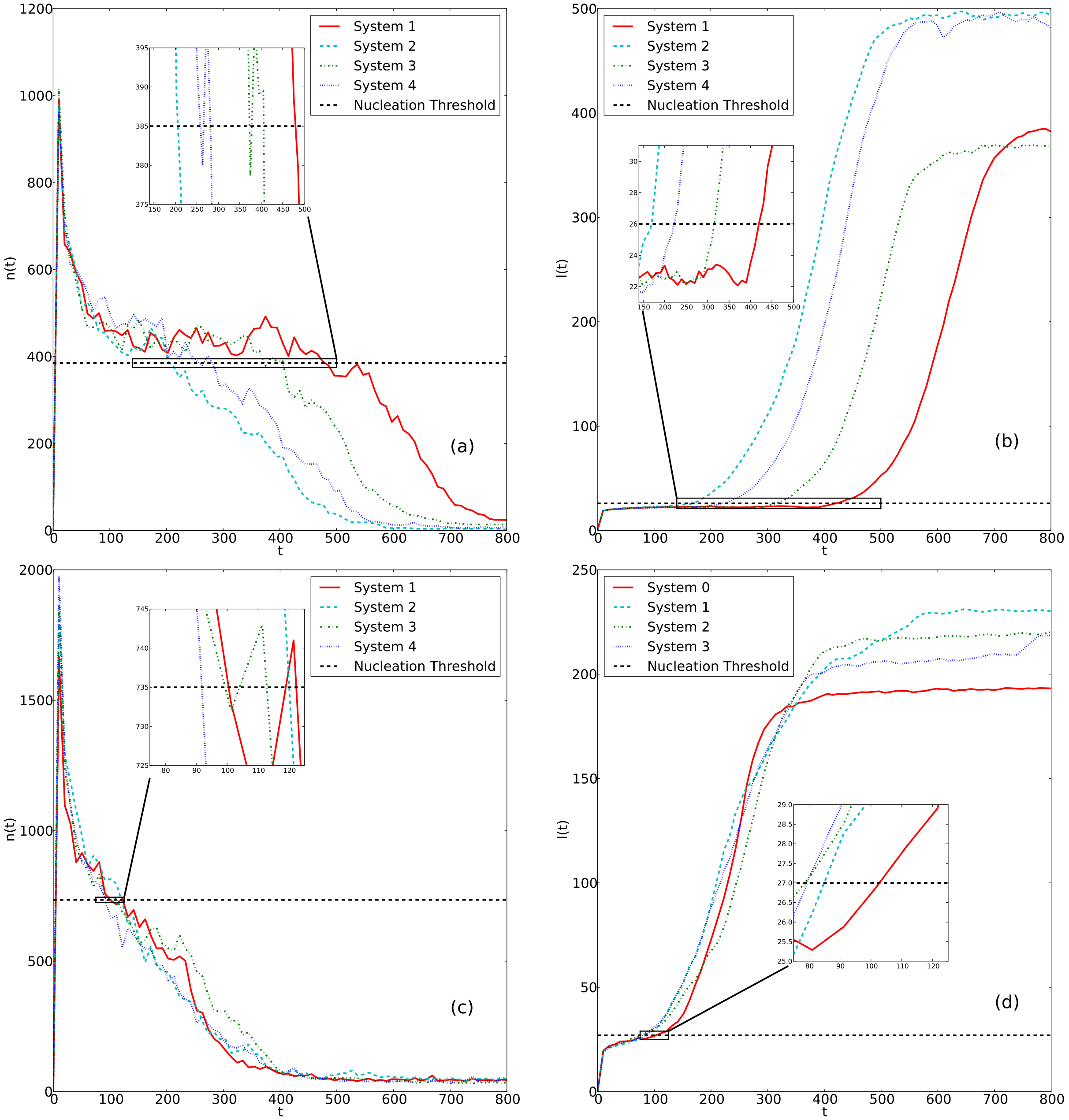

Figure 4.1: (a), (c): Number of topological defects $n(t)$ and (b), (d) numerically determined characteristic length scale $l(t)$, determined from the mean shock front distances, as functions of numerical simulation time t, for systems with control parameter pairs $b = -3.5$, $c = 0.556$ (a), (b); $b = -3.5$, $c = 0.44$ (c), (d). The different graphs (with distinct colors) represent four independent realization runs. The estimated nucleation threshold values for each plot were chosen ad hoc “by hand and eye”: (a): $n_{\text{th}} = 385.0$; (b): $l_{\text{th}} = 26.0$; (c): $n_{\text{th}} = 735.0$; (d): $l_{\text{th}} = 27.0$.

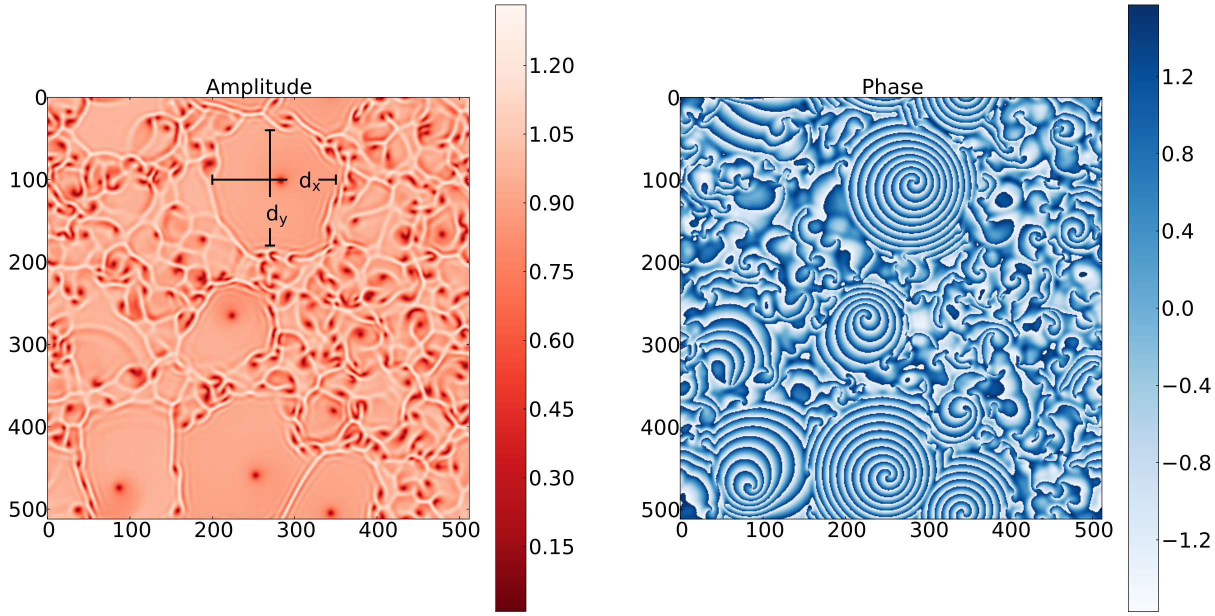

Figure 4.2: Amplitude (red-white, left panel) and phase (white-blue, right panel) plots of the complex order parameter A, for control parameters $b = -3.5$, $c = 0.44$. The darkest points in the amplitude plot indicate the topological defects for which $|A| = 0$, while the lightest color (almost white) here indicates the shock line structures with steep amplitude gradients. The spiral structures are clearly visible in the phase plot within the domains separated by the shock fronts.

from defect turbulence to the frozen state; and (c,d): $b = -3.5$, $c = 0.44$, which represents a location deep within the frozen region. In Figs. 4.1(a,c), we show the measured decaying defect number $n(t)$ as function of time for four independent simulation runs (starting from different random initial configurations). The black dashed lines indicate the estimated nucleation thresholds, here simply determined by visual inspection of the graphs (below, we shall propose a more systematic approach to obtain this threshold and describe it via a phenomenological formula). Due to the large fluctuations of those individual time tracks $n(t)$, they may intersect the supposed threshold line multiple times, leading to considerable ambiguity in the measurement of associated nucleation times. One may of course reduce the relative fluctuations through running a multitude of independent numerical integrations and thus improve the statistics, yet at marked increase in computational expenses.

In order to overcome this difficulty, we propose an alternative method to extract a relevant characteristic length scale $l(t)$ directly, which is much less affected by stochastic fluctuations and consequently displays improved monotonic behavior during the nucleation process. To this end, we recall that the final states reached after nucleation are stationary, typically square- or pentagon-shaped single-spiral domains, which are well-separated by shocks. Hence we choose the average size of those domains, or equivalently, the initially growing mean distance between shock fronts, to represent a useful quantitative measure for a characteristic length scale in such CGL systems. Specifically, we compute the distance between all pairs of adjacent shock lines both along the x and y directions in the amplitude plots (e.g., shown in the left panel of Fig. 4.2); their average serves as a direct measurement of the time-dependent characteristic length scale in our system.

More details of the this method are illustrated in Fig. 4.2 [137]: We first select a point and measure both d_x and d_y respectively (the selected point thus is the intersection of the two depicted black lines). We then repeat this process by scanning all points in our square lattice and simply compute the average of all d_x and d_y values, yielding an estimate for the characteristic length scale $l(t)$. Some preliminary measurements of this quantity for the same systems for which we determined the decaying defect number $n(t)$ are shown in Fig. 4.1(b,d) as well. We make the following pertinent observations: First, the mean separation distances between defects $l_{\mathrm{sep}}(t)$ following from the data in graphs (a,c) roughly follow the behavior of the curves (b,d). The data for the characteristic lengths $l(t)$ in Fig. 4.1(b,d) are however clearly subject to much lower fluctuations, and from the curves' intersection with the set threshold lines allow markedly better defined estimates for nucleation times for the onset of stable spiral structures, even near the strongly fluctuating transition regime (b). Yet this also implies that the characteristic length scale $l(t)$ is quite sensitive to those nucleation processes, and a careful analysis of the entire evolution history for the complex order parameter $A(\boldsymbol{x}, t)$

is required to appropriately select the proper nucleation threshold.

We shall subsequently apply the method described above to determine the growing length scales in two-dimensional CGL systems, and utilize these to further characterize nucleation processes as follows: First of all, we carefully investigate the evolution histories of both the phase and amplitude of the complex field $A(\boldsymbol{x}, t)$ on the square lattice, and select a tentative threshold l_{th} according to these investigations. Next, we collect statistically significant data, and employ this prior selected length to monitor nucleation processes: When the characteristic length $l(t) > l_{\mathrm{th}}$ exceeds the set threshold, we assume a spiral structure to have successfully nucleated. The spiral associated with this nucleation will then expand, and ultimately either fill the entire two-dimensional system by itself or jointly with other spiral domains. We hence measure the time difference from the very beginning of the numerical simulation ($t = 0$) until $t = T_n$ where $l(T_n) \geq l_{\mathrm{th}}$, and collect the resulting time interval data T_n for further analysis: In order to eliminate inaccuracies introduced by our ad-hoc choice of the nucleation threshold size l_{th} as well as finite-size effects, we examine the dependence of the associated dimensionless nucleation barrier on l_{th} and L with the aid of a phenomenological formula, and finally extract an extrapolated critical nucleus size and barrier (details will be described in the following section 4.4). We repeat these procedures and data collection with ensuing analysis for different selections of parameter pairs (b, c) according to their distance to the transition line where the defect turbulence regime becomes meta-stable; these various scenarios will be discussed in the following section.

Furthermore, since target wave patterns display quite similar shock structures as the spiral structures in the frozen state, we may also characterize the characteristic length scale of the corresponding CGL systems and their nucleation dynamics in section 4.5 in a similar manner.

4.4 Spiral Structure Nucleation

We now proceed to explore spiral structure nucleation processes in two-dimensional CGL systems, for two representative different parameter pairs (b, c). Specifically, we quench the control parameters to values that correspond to states that are situated either deep in the frozen region, or close the transition or crossover line where defect turbulence becomes metastable [137]. These two quench scenarios present distinct challenges to the subsequent statistical analysis, which hence needs to be performed carefully. In order to obtain robust conclusions, we gather data with sufficient statistics from many numerical integrations with different initial conditions for various system sizes L, which may subsequently allow us to extrapolate to the infinite-system limit.

4.4.1 Quench Far Beyond the Defect Turbulence Instability Line

We begin with quenches of the control parameters ($b = -3.5$, $c = 0.44$) deep into the stable frozen-state regime, for which nucleation processes should happen comparatively fast, hence requiring less computation time. Furthermore, since the eventual frozen configurations are usually occupied by multiple spirals [137], finite-size effects can be at least approximately eliminated through extrapolation to the $L \to \infty$ limit.

A histogram plot for the normalized nucleation time distribution for different linear system sizes L is shown on the left panel in Fig. 4.3. The tentative threshold length employed here is $l_{\text{th}} = 27$, which is simply chosen by inspection of $l(t)$ time track data, see Fig. 4.1(d). The nucleation time distributions for these different systems look quite similar, but display steeper and sharper peaks as the system size increases, as one would expect: Smaller systems are more strongly affected by finite-size effects, which tend to broaden the distribution. Moreover, as also observed in the previous study [78], we find that the total number of

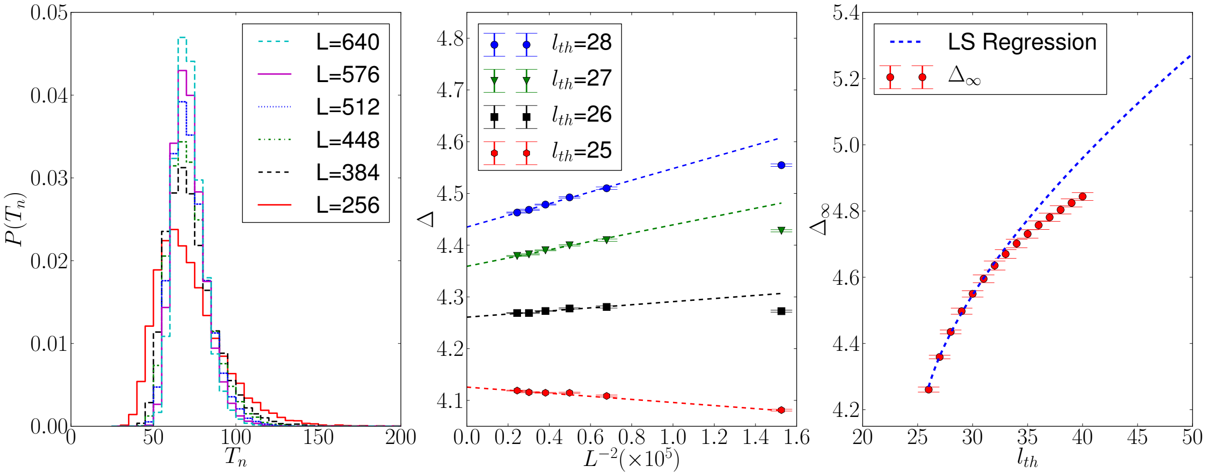

Figure 4.3: (Left) Normalized distribution (histogram) $P(T_n)$ of measured nucleation times T_n for two-dimensional CGL systems with $b = -3.5$, $c = 0.44$ and different sizes (varying from 256×256 to 640×640); here we set $l_{\text{th}} = 27$ and ran $20,000$ realizations for each system size. (Middle) Extracted dimensionless nucleation barrier Δ as function of the inverse system size L^{-2} utilizing different values for the tentative threshold l_{th}; the dashed lines indicate a least-square fit for the data points with the four largest system sizes. (Right) Infinite-size limit ($L \to \infty$) barrier Δ_∞ vs. the prior selected threshold length l_{th}; the (blue) dashed line shows the least-square fit to Eq. (4.9) using the seven data points with the smallest threshold lengths.

defects increases with growing system size, whence multiple nucleation events may happen simultaneously for larger systems. With increasing L, a slight shift of the peak to larger nucleation times is also noticeable in our data, which can be viewed as evidence for imperfect threshold length selection. Indeed, a threshold length that renders the average nucleation time $\langle T_n \rangle$ size-invariant should constitute at least a temporary optimal choice. We thus collected data for multiple selected tentative threshold lengths l_{th} for otherwise identical system in our numerical experiment.

We proceed drawing an analogy with nucleation at first-order phase transitions in equilibrium, where thermal fluctuations may help a nucleus beyond a critical size to overcome the free-energy barrier between the metastable and stable states. For the CGL, we take the intensity of stochastic fluctuations in the defect turbulence regime to play the role of temperature, and also assume that nucleating stable spiral structures requires the system to overcome an effective barrier. However, in this far-from-equilibrium system, we cannot easily quantify an effective temperature nor uniquely determine a free-energy landscape. We may however introduce an effective dimensionless nucleation barrier Δ, which we simply define via the following connection with the average transition time $\langle T_n \rangle$:

$$\langle T_n \rangle = e^{\Delta} \tag{4.8}$$

(in units of simulation time). Furthermore, in metastable systems finite-size effect play a crucial role, as observed in numerous numerical studies.

In the following, we describe our data analysis procedure that allows us to successfully eliminate or at least drastically mitigate finite-size corrections: First, we propose a straightforward relation between the numerically extracted barrier from Eq. (4.8) and the system size L^2:

$$\Delta \approx C_L L^{-2} + \Delta_{\infty}, \tag{4.9}$$

i.e., we assume the finite-size corrections to scale inversely with the system size; this linear dependence of Δ on L^{-2} is in fact confirmed in our data for sufficiently large L in the middle panel of Fig. 4.3 for four different threshold values. Since the first term here vanishes as $L \to \infty$, Δ_∞ corresponds to the effective dimensionless barrier in the thermodynamic limit.

Second, we wish to eliminate ambiguities and uncertainties related to our ad-hoc choice of the threshold length l_{th} used to measure the nucleation times. Indeed, the extrapolated value for Δ_∞ does depend significantly on the selection of l_{th}, as is evident in the middle panel of Fig. 4.3: A larger threshold length implies bigger nucleation droplet size, the formation of which definitely requires longer time. Yet we may immediately rule out some choices first based on Eq. (4.9); for example, when $l_{\text{th}} = 25$, we find a negative slope ($C_L < 0$) which contradicts the basic assertion that activation barriers should become entropically reduced in larger systems; therefore, we may consider $l_{\text{th}} = 25$ an inappropriate choice. Indeed, since our goal is to also eliminate finite-size effects inasmuch as at all feasible, it appears natural to pick a threshold length criterion that will provide us with a size-invariant mean nucleation time. For the data displayed in the middle panel of Fig. 4.3, we infer that this optimal threshold l_c should lie in the range $(25.0, 26.0)$, but closer to the upper bound, according to the slope of the four dashed lines. One might thus iterate the above simulation steps to further confine the interval for an optimized l_c; however, this procedure would be computationally quite expensive, and also impeded by sizeable statistical errors that render distinctions between almost flat functions $\Delta(L^{-2})$ very difficult.

We therefore propose an alternative approach in postulating a purely phenomenological formula to model the relationship between the extrapolated Δ_∞ and l_{th}:

$$\Delta_\infty(l_{\text{th}}) = \Delta_0 + \Delta_1 \left(l_{\text{th}} - l_c\right)^\theta \ , \tag{4.10}$$

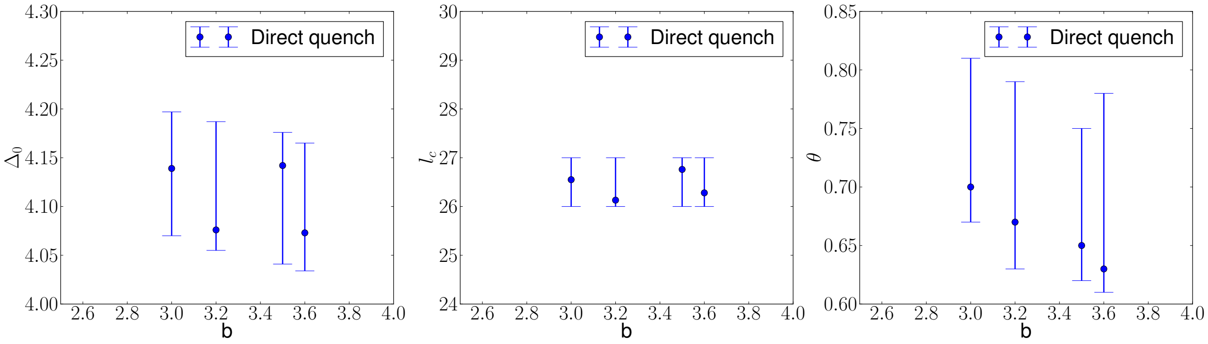

Figure 4.4: From left to right: size-invariant dimensionless barrier Δ_0, critical threshold length l_c, and exponent θ as functions of the control parameter b, with $c = -0.40$ held fixed. These quantities are extracted by fitting our numerical data to the empirical formula (4.10); the label "Direct quench" indicates that the CGL systems here are directly quenched from random initial configurations into the frozen regime.

which empirically fits our data quite well for $l_{\rm th} \approx l_c$, as shown in the right panel of Fig. 4.3. Naturally, we would expect Eq. (4.10) to hold only when $l_{\rm th} \approx l_c$, and consequently restrict our subsequent data analysis to this regime where the results are nearly independent of the originally selected threshold length $l_{\rm th}$. We note that selecting a too large value for $l_{\rm th}$ would bias configurations towards super-critical nuclei, which essentially have already reached the frozen state. Similarly, when estimating our error bars for, e.g., the least-square fits to our empirical formula (4.10), we give more weight to the data points closer to l_c.

We have applied the data analysis method described above to investigate representative CGL parameter pairs (b, c). In order to check for systematic dependencies, we hold either b or c fixed, and vary the other control parameter, to yield two complementary data sets. Since we investigate the focusing quadrants with $bc < 0$, we may utilize the fundamental gauge symmetry $(A, b, c) \to (A^*, -b, -c)$ to restrict ourselves to fixing either $b < 0$ with varying $c > 0$, or vice versa. Figures 4.4 (for fixed $c = -0.4$) and 4.5 (with fixed $b = -3.5$) show our results for Δ_0, l_c, and θ in Eq. (4.10) for each parameter set. In both sets of parameters, upon increasing $c > 0$ or $b > 0$, respectively, the system approaches the transition line beyond which persistent defect turbulence is stabilized [7].

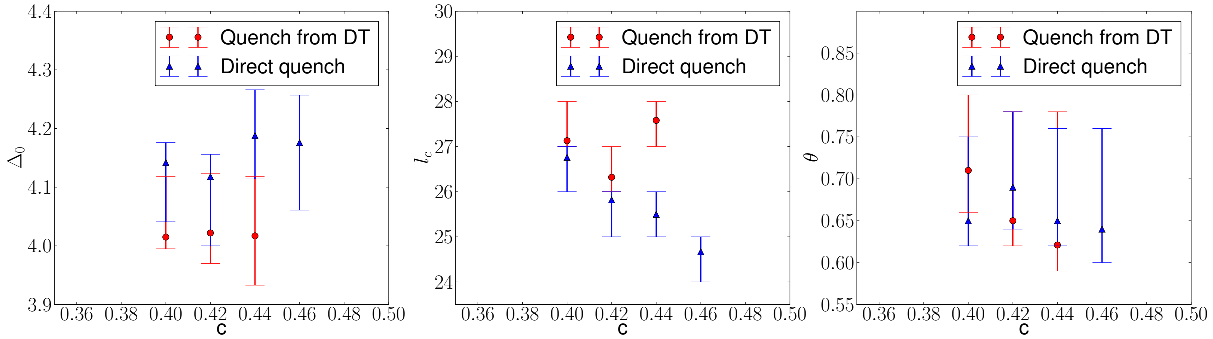

Figure 4.5: From left to right: size-invariant dimensionless barrier Δ_0, critical threshold length l_c, and exponent θ as functions of the control parameter c, with $b = -3.50$ held fixed. The label “Quench from DT” (data plotted in red) indicates that these systems were initialized in the defect turbulence regime with $b = -3.4$ and $c = 1.0$, remained in this phase for a simulation time interval $\Delta t = 50$, and were subsequently quenched into a frozen state characterized by the parameter pairs (b, c) listed.

We first observe that the extracted dimensionless nucleation barriers Δ_0, which according to our analysis should be essentially independent of the choice of the threshold length and effectively represent values extrapolated to infinite system size, appear to display no statistically significant dependence either on our adjusted sets of parameter values b or c, but merely fluctuate around $\Delta_0 \approx 4.15$. This robust positive value is likely a consequence of the fact that those parameter pairs reside far away from the crossover limit. Hence the meta-stable transient turbulent state observed in Ref. [78] does not become apparent, and our systems directly nucleate from the imposed fully random initial configurations to persistent spiral structures in the frozen state with typical nucleation times that do not differ markedly for the parameter range tested here. Thus, within the parameter ranges explored in this work, it appears that the effective extrapolated nucleation barrier Δ_0 remains positive, and based on the absence of any noticeable decrease upon approaching the instability line of the defect turbulence state, we conjecture that it remains non-zero throughout the frozen (or “vortex glass”) state. This would imply that the transition from defect turbulence to the frozen state is discontinuous. Indeed, in our data in Fig. 4.5 for fixed $b = -3.5$, one might even discern that Δ_0 rather slightly grows with increasing c, which may indicate an enhanced effective surface tension. However, fluctuations also become larger upon approaching the transition limit, and we would need much improved statistics to make a definitive conclusion.

Second, we find the extracted threshold lengths l_c that consistently monitor the nucleation for different system sizes to slightly drop with increasing $c > 0$ for fixed $b < 0$, see Fig. 4.5, while they remain constant within our error bars as function of $b > 0$ for fixed $c < 0$, Fig. 4.4. This observation may be explained through the fact that upon varying the parameter c from $c = 0.4$ to $c = 0.46$ at constant $b = -3.5$, one approaches the transition regime faster, and comes closer to it, than for the explored b range at constant $c = -0.40$. Third, we do not discern significant systematic variations of the fit exponent θ in Eq. (4.10) with b or c, see the left panels of Figs. 4.4 and 4.5; within our numerical accuracy, this exponent appears universal for the frozen states with the distinct parameter pairs investigated here.

As mentioned above, our results for the spiral structure nucleation processes appear at variance with the findings in Ref. [78]. The main reason for this discrepancy is that we consider quenches of our system much deeper into the frozen regime, whence we do not observe meta-stable defect turbulence states. Our data consequently do not allow us to decouple the initial decay process, suggested by Huber et al., from the actual nucleation process that overcomes the barrier. For the cases studied here, the transient relaxation kinetics is obviously fast, and we may therefore simplify our nucleation time measurements by simply combining these two processes. In order to check if this simplification is adequate, we have applied a different quench protocol to investigate nucleation into frozen spiral structures: Namely, instead of directly adjusting the parameter pair (b, c) to the frozen state regime, we first quench the system to the defect turbulence region. We subsequently run its dynamics sufficiently long for the system to reach a stationary (quasi-stable) turbulent state with roughly constant density, and only then quench the system again into the frozen state regime.

Thus we first explicitly set the system up in the defect turbulence region, and later let the spiral structures nucleate from this configuration.

We apply the same techniques as previously to analyze spiral structure nucleation processes in this scenario, except that the nucleation time is now measured as the elapsed interval after performing the second quench. We choose the corresponding control parameter pair for the explicit defect turbulence state uniformly as $b = -3.4$ and $c = 1.0$. Yet there is of course still stochastic variability for the ensuing nucleation processes; hence we test three pairs of control parameters, namely $(b, c) = (-3.5, 0.4)$, $(-3.5, 0.42)$, and $(-3.5, 0.44)$. Inspection of the resulting data yields that the explicit defect turbulence intermediate state merely causes an overall shift of the nucleation time distribution towards lower values; and this offset turns out small compared with the average nucleation time. The associated size-invariant nucleation barriers Δ_0, the critical threshold lengths l_c, and fit exponents θ are shown (as red data points) in Fig. 4.5. The thus extracted dimensionless nucleation barrier values are consistent with the direct quench results within our error bars. This suggests quite similar nucleation kinetics starting from either random initial configurations or from a pre-arranged defect turbulence state. Therefore, our discontinuous transition conclusion should hold even if one explicitly decouples the initial decay from random initial configurations from the subsequent relaxation from the defect turbulence state, at least in this deep-quench scenario. We do however observe deviations in the measured optimal critical threshold lengths (middle panel in Fig. 4.5) for these two quench strategies, with the data obtained from the case with intermediate defect turbulence states resulting in slightly larger and more uniform values for l_c. Apparently, these minor variations in the critical threshold l_c do not strongly affect the extracted size-invariant barriers $\Delta_0 \approx 4$, which show no tendency to decrease upon approaching the instability line.

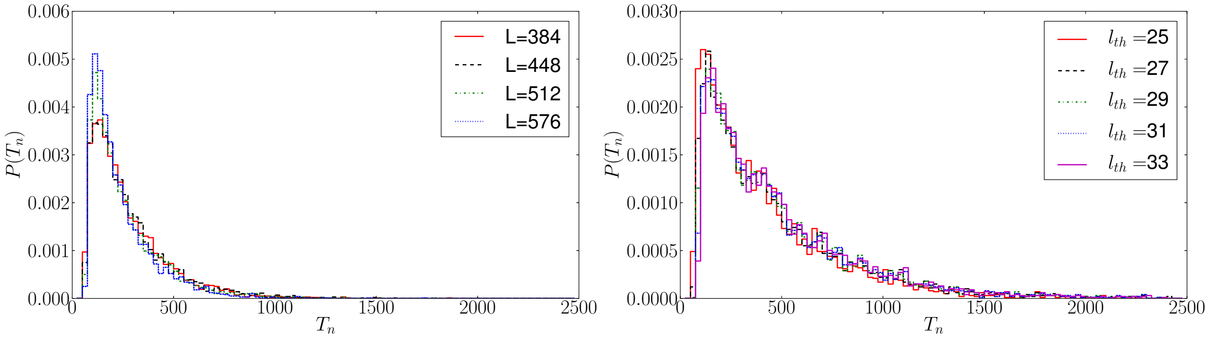

Figure 4.6: Normalized nucleation time distributions $P(T_n)$ for two-dimensional CGL systems with $b = -3.5$ and $c = 0.556$. Left panel: Data for varying the system size L^2 from 384×384 to 576×576, with ad-hoc selected nucleation threshold length $l_{\text{th}} = 24$. Right panel: Histograms for different nucleation thresholds l_{th} at fixed system size $L = 384$; $4,000$ independent realizations were run until simulation time $t = 2400$ for each histogram.

4.4.2 Quench Close To the Instability Line

Next we proceed to investigate a parameter quench close to the transition line [137], applying similar numerical methods. When approaching the crossover regime, as shown in Fig. 4.1(a,b), a meta-stable state with a well-defined topological defect density and corresponding characteristic droplet size is formed. However, the proximity to the instability regime in the b-c parameter space induces much larger fluctuations than in the deep-quench scenario of the previous subsection. Therefore, a wider nucleation time distribution with larger mean is to be expected in this case. Indeed, this prediction is borne out by our simulations, for which we gathered data for quenches to the control parameter values $b = -3.5$ and $c = 0.556$, exactly the same as used in Fig. 4.1, with comparatively lower statistics ($4,000$ realizations were run for each distribution). The resulting normalized nucleation time histograms are displayed in Fig. 4.6 for various system sizes L (left panel) and different choices for the threshold length l_{th} (right panel).

We note that there is no significant difference visible between between the nucleation time histograms in the left panel of Fig. 4.6 for the data obtained with linear system sizes $L = 384$

and 448, in contrast with the results shown in Fig. 4.3 for quenches far beyond the transition line. Even the two distributions for the larger size curves $L = 512$ and 576 do not differ very much from those for smaller systems. The reason for this distinct behavior is, perhaps counter-intuitively, a larger finite-size effect in this present case: Indeed, most of the CGL systems in domains of size 384×384 or 448×448 will actually in the end be occupied by a single large spiral, owing to stronger fluctuations and lower nucleation probabilities. Therefore, the ensuing nucleation distributions are quite similar, while the two bigger simulation domains may accommodate perhaps two or three spiral structures, resulting in slightly narrower and sharper peaks in the associated nucleation time distributions. These observations unfortunately render the extrapolation method detailed in the previous subsection impractical in the present situation, as this would require runs on prohibitively much larger systems which exceeds our current computational resources. Furthermore, the rather small differences between the nucleation time distributions obtained for different pre-set threshold lengths (right panel) do not allow systematic studies of the dependence on l_{th} either. Consequently we focus on characterizing the long, "fat" tail in the nucleation time distributions instead, which were in fact comparatively insignificant in the deep-quench scenario. Hence we now restrict ourselves on relatively small systems with $L = 384$, for which the final quasi-stationary state most likely contains a single spiral, but measure the nucleation time distribution for fixed size and a single set nucleation threshold $l_{\mathrm{th}} = 24$ with the same control parameters, but with much better statistics, namely running $40,000$ independent realizations; the resulting histogram is depicted in Fig. 4.7. As shown in the middle panel, the decaying part of this nucleation time distribution is well-described by a simple exponential form

$$P(T_n) \propto e^{-T_n/\tau}, \tag{4.11}$$

as is further confirmed by the double-logarithmic fit for the long-time "fat" tail in the right

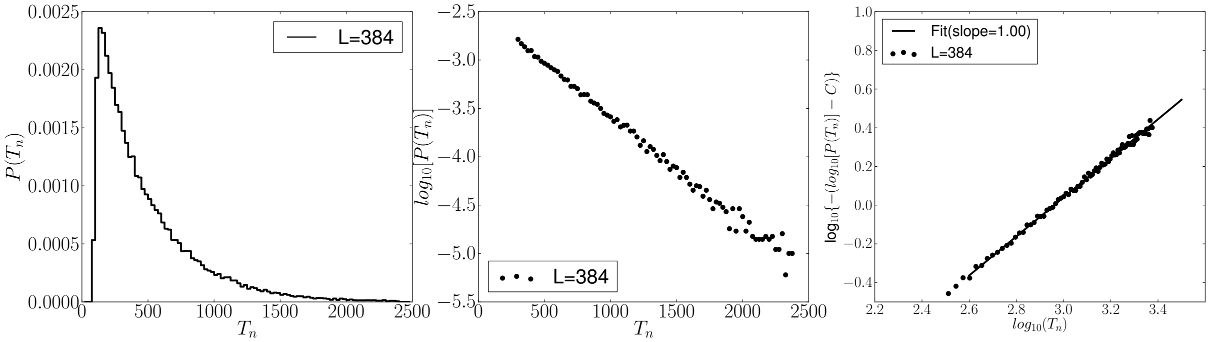

Figure 4.7: Normalized nucleation time distribution $P(T_n)$ for two-dimensional CGL systems with $b = -3.5$, $c = 0.556$, linear system size $L = 384$, and nucleation threshold length $l_{\text{th}} = 24$; $40,000$ independent realizations were run until simulation time $t = 2400$.

panel; i.e., our measured nucleation time can be viewed as an exponentially distributed random variable in the long tail regime. We point out that a nucleation study in the meta-stable region for a two-dimensional ferromagnetic Ising spin system with Glauber dynamics in systems subject to a polarizing magnetic field at zero temperature yielded very similar results [139]. For that model, the normalized nucleation time of a single rectangular droplet of positive spins in a bulk region of opposite alignment has been proven to represent be a unit-mean exponentially distributed random variable. This fact in turn is a consequence of the discontinuous nature of the phase transition separating both ferromagnetic configurations below the critical temperature upon tuning the magnetic field. The average lifetime of the metastable state is also rigorously shown to satisfy Eq. (4.8) with appropriate free-energy barrier relative to $k_{\text{B}}T$ [140], consistent with our conclusion in subsection 4.4.1.

It should however be noted that our CGL nucleation processes are not completely captured by this equilibrium asymptotic analysis, and our measured nucleation time distributions are not perfectly exponential, in neither of the quench scenarios discussed above. This is due to several facts: First of all, for systems that are quenched from random initial configuration, there exists a finite initial decay interval until they attain a meta-stable state. This was pointed out by Huber et al. [78], who consequently applied an overall time shift for the nucleation histograms. Second, finite-size effects clearly affect numerically obtained nucleation time distributions. As is apparent in the left panel of Fig. 4.6, the function $P(T_n)$ approaches an exponential shape for larger systems, and its rising flank tends to disappear as $L \to \infty$. For quenches close to the instability line, computational limitations prevent us from systematically eliminating finite-size effects. On the other hand, CGL configurations quenched far beyond the crossover regime are characterized by separate spiral droplet domains that are separated by sharp shock fronts. These structures are very stable, at least in simulations with finite system sizes, and hence effectively prevent the merging of individual spirals to form increasingly large droplets. Consequently, the CGL systems indeed become "frozen", in stark contrast with the slow coarsening kinetics in the ferromagnetic Ising spin system.

4.5 Target Wave Nucleation

Upon introducing an appropriate localized inhomogeneity, one may trigger target wave patterns for the CGL [137]. These small inhomogeneous spatial regions then play the role of pacemakers, which locally alter the oscillation frequency [141]. Another useful analogy is to view the small inhomogeneous regime as a slit, whence target wave patterns can be interpreted as diffraction phenomena. Thus the spatial extend of the inhomogenity should be comparable to the wave length of the resulting target structure. In contrast to the spiral waves discussed in the previous section, target waves carry zero topological charge $n = 0$.

In the following, we explore transient kinetics in the formation of target waves, and indeed characterize it in terms of nucleation dynamics, applying the same techniques as detailed above for incipient spiral structures. To this end, we set our CGL simulations up as follows: We initiate them with fully randomized configurations, and select control parameters according to previous work that aimed to control defect turbulence by means of target waves

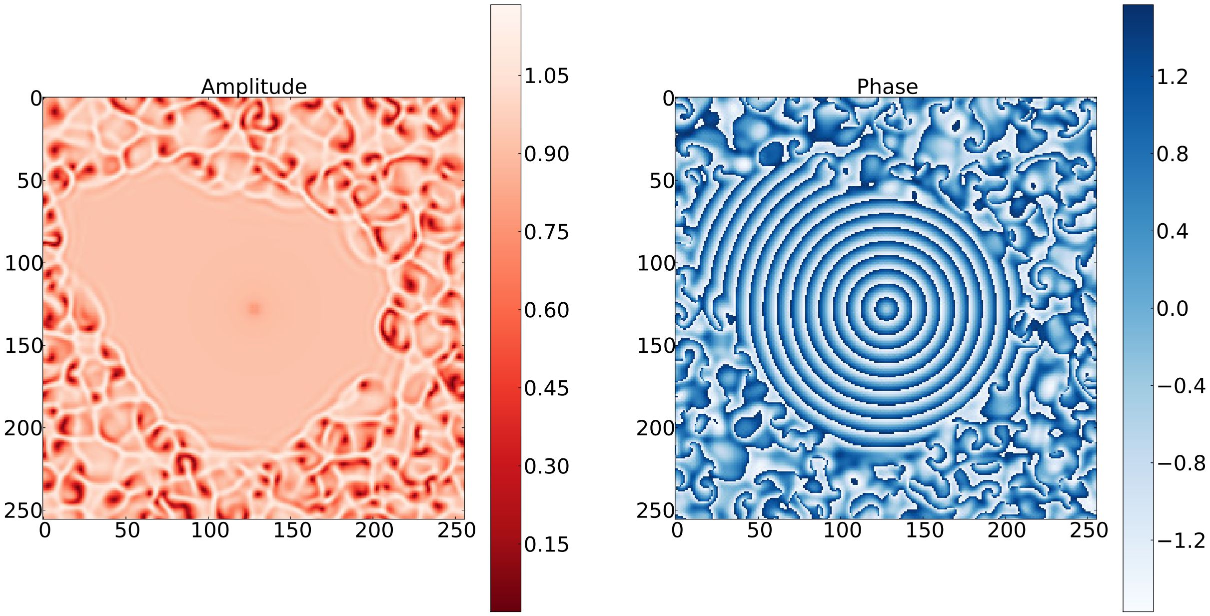

Figure 4.8: Amplitude (red-white, left panel) and phase (white-blue, right panel) plots of the complex order parameter A, with bulk control parameters $b = -1.4$, $c = 0.9$ in a 256×256 system; in the central 4×4 block, instead $b = -1.4$, $c = 0.6$ (discernible as the small square structure with different coloring in the center). The configuration is shown at numerical time $t = 1200$; in the left panel, the lightest color (almost white) indicates shock line structures with steep amplitude gradients.

[106], namely we fix $b = -1.4$ over the whole system, and set $c = 0.9$ to obtain an absolutely unstable defect turbulence configuration, except for a "central" patch of 4×4 sites, where $c = 0.6$, which corresponds to a stable frozen state. We remark in passing that other inhomogeneities may also generate target waves, as investigated in Ref. [105]. There, however, the basic Eq. (4.2) becomes modified by an addition to the imaginary part in the coefficient of the linear term which causes an explicit frequency shift. In this case, there exist two different types of target wave solution; we will however not consider this type of inhomogeneity as the ensuing phenomenology cannot be directly compared with our spiral nucleation study.

With the setup described above, a target wave oscillating with the pacemaker's frequency becomes spontaneously excited, after sufficient computation time has elapsed. Furthermore, the number of target wave structures is determined by how many distinct impurity regions are introduced. An example for a resulting coherent structure is depicted in Fig. 4.8, for which a single local inhomogeneity was implanted, whence exactly one emergent target wave is expected. The existence of the shock-line structures separating the near-circular target waves from the surrounding defect turbulent state ensure that our method to monitor nucleation events using a characteristic growing length scale $l(t)$ is applicable here as well. However, close observation of the temporal evolution of this target wave structure invalidates our strategy of section 4.4.1 to extract an invariant threshold length. Due to the significant spatial asymmetry for the target wave expansion into its turbulent environment, there is a fair chance that the initiated droplet structure may suddenly shrink and subsequently attempt to reform towards a more symmetric droplet shape. This leads to significant non-monotonic variations in the characteristic droplet size, and concomitant ambiguity in determining any incipient nucleation event. We note that this phenomenon may be associated with the fact that the inhomogeneity is introduced by hand, as well as the imposed periodic boundary conditions. Furthermore, the nucleation of target wave droplets is markedly more difficult

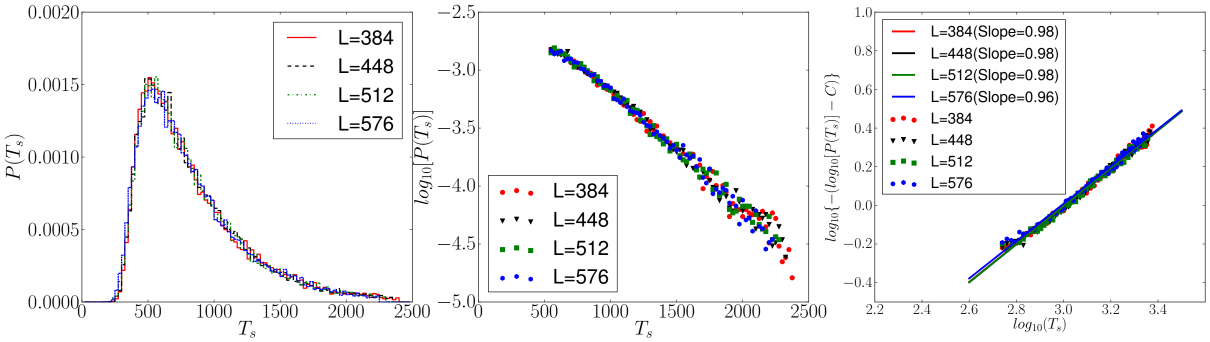

Figure 4.9: (Left) Normalized nucleation time distribution $P(T_s)$ for two-dimensional CGL systems with bulk control parameter values set to $b = -1.4$ and $c = 0.9$, whereas $c = 0.6$ in the central 4×4 patch, for varying linear system size ranging from $L = 384$ to 576. T_s represents the measured nucleation time adjusted by a size-dependent shift in order to achieve data collapse; we set the nucleation threshold length to $l_{\text{th}} = 17.0$, and ran 20,000 independent realizations for each system size.

than that of spiral structures as investigated in section 4.4, since there is now only one pre-assigned nucleation center, and the surroundings, which reside in a stable defect turbulence state, are subject to stronger fluctuations. Consequently we proceed to tentatively investigate target wave nucleation processes with a single ad-hoc selected nucleation threshold, under the assumption that this will suffice to characterize the system's time evolution, similar as in section 4.4.2 for spiral structures in the near-instability quench scenario.

Our measured nucleation time distributions, obtained for different system sizes with 20,000 runs for each L, are shown in Fig. 4.9. As anticipated, the typical nucleation times for the target waves are much longer than those for spiral structures. In fact, some simulation runs did not lead to successful nucleation events by the time $t = 2,400$ when our runs were terminated. Hence, the actual number of realizations over which the data were averaged are actually different for each system size, as listed in Table 4.1. Upon increasing L, we observed a manifest shift to higher values in the directly measured nucleation times, which reflects the enhanced stability of the bulk defect turbulence regime with growing total system size at fixed spatial extent of the central nucleation inhomogeneity. Correspondingly, we detect a slight decrease in the number of successful nucleation incidents (Table 4.1). In order to facilitate the comparison of data resulting from the different system sizes, we have shifted the nucleation time histograms by hand to collapse them on top of each other. Aside from that overall shift, these distributions (as functions of the shifted nucleation times T_s) are quite similar because of the identical nucleation centers. Furthermore, they display long, fat tails in the large-time regime, akin to spiral droplet nucleation for quenches close to the transition line in parameter space. Indeed, as in that quench scenario, the CGL systems dominated by target waves are ultimately also occupied by a single droplet structures, since of course only one inhomogeneous nucleus was placed in the simulation domain. The large-T_s tails are again of an exponential functional form, as demonstrated by the logarithmic and double-logarithmic data plots in Fig. 4.9. This remarkable consistency between spiral structure and target wave nucleation may be explained in a natural manner by simply viewing the latter as externally stabilized structures with topological charge $n = 0$ [105], akin to spiral waves with $n = \pm 1$, whence their nucleation events display similar exponential statistics.

System size	Number of nucleated systems
384×384	$19,792$
448×448	$19,733$
512×512	$19,732$
576×576	$19,589$

Table 4.1: Number of systems that have nucleated successfully by computation time $t = 2,400$ among $20,000$ independent realizations for different system sizes.

4.6 Conclusions

We have studied the transient dynamics from the defect turbulence to the frozen state in the two-dimensional CGL. To this end, we have numerically solved the CGL equation explicitly on a square lattice, and investigated the associated nucleation process of stable spiral as well as target wave structures, which eventually dominate the whole two-dimensional domain when the quasi-stationary frozen state is reached [137]. In order to quantitatively and reliably characterize the nucleation kinetics, we have proposed a computational method to systematically extract the characteristic nucleation lengths for various parameters in the CGL systems, which signify the typical size of incipient droplet structures in the amplitude field of the complex order parameter. We have collected sufficient data and for various system sizes to ensure decent statistics, and in the deep-quench scenario allow for extrapolation to infinite system size.

For the spiral droplet nucleation study, we prepare our system with random initial configurations and quench it to the meta-stable defect turbulence regime in control parameter (b, c) space, in two scenarios either near and far away from the transition or crossover line to the frozen region. By means of our extrapolation method and proposed phenomenological formula to eliminate artifacts related to the choice for the nucleation threshold as well as finite-size effects, we have extracted a finite effective dimensionless nucleation barrier for CGL systems that are quenched far away from the instability line. We posit that this non-zero, and approximately constant nucleation barrier indicates a discontinuous transition from the defect turbulence to the frozen state displaying persistent stationary spiral structures. We have found indications that this conclusion holds for various quenches into the defect turbulence region with different system control parameters, and it appears that the fit exponent θ in Eq. (4.10) might be universal as well. In addition, we have considered a distinct quench scenario with an intermediate explicit turbulent state to evaluate the effect of quite different initial conditions on the ultimate spiral nucleation processes. We have detected only minor differences in both critical nucleus sizes and effective nucleation barriers between both situations, apparently confirming a robust discontinuous transition picture.

On the other hand, for quenches to regions located near the transition line in parameter space, we obtain an exponential decay in the measured nucleation time distributions, with long “fat” tail. This finding is remarkably similar to spin droplet nucleation in ferromagnetic spin systems with non-conserved Glauber dynamics in finite two-dimensional lattices with periodic boundary conditions subject to a polarizing external field in the zero-temperature limit. Drawing this analogy provides us with additional evidence for our discontinuous transition conclusion, despite obvious differences between nucleation processes in two-dimensional non-equilibrium CGL systems and such equilibrium ferromagnetic lattices. The results from our combined two different quench scenarios reinforce our conclusion that the transition between the defect turbulence and spiral frozen states is likely discontinuous.

Finally, we have investigated nucleation processes for different patterns that can be also observed in some experimental systems, namely target waves. In this situation, in the eventual frozen state our systems become filled with target wave rather than spiral structures in the phase map of the order parameter, which also are droplet-like in the associated amplitude field. To trigger the nucleation process for target waves, one needs to introduce some specific inhomogeneity into the two-dimensional CGL systems. (We note that there also exist other methods to generate target wave structures [142] which are beyond the scope of this paper.)

We have applied the same analysis method as for our spiral-wave nucleation study in the near-transition line quench case, and arrive at the remarkable conclusion that the nucleation kinetics in these two very distinct situations, leading to rather different final wave structures, are in fact quite similar: Again we observe an exponential distribution for target wave nucleation, accompanied by the characteristic long fat tails that are indicative of an associated discontinuous transition from the defect turbulence to the frozen state. We hope that similar methods will be utilized in the future, perhaps with improved and more powerful computational resources, to quantitatively explore and robustly characterize nucleation features for both the CGL as well as other stochastic non-linear dynamical systems.

Chapter 5

Conclusions

We presented three studies in this dissertation investigating the complex Ginzburg-Landau equation by means of different approaches: Chapters 2 and 3 focus on initial-slip and aging phenomena when the system is quenched either at the critical point or below the critical point, while Chapter 4 discusses nucleation processes for spiral or target wave structures when transitions are induced from the "defect turbulence" state to a dynamically frozen state. All these three studies reveal interesting transient dynamical properties of the complex Ginzburg-Landau equation.

Employing the perturbative field-theoretic renormalization group method we investigated the critical initial-slip scaling behavior in the complex Ginzburg-Landau equation with additive noise analytically. The initial-slip exponent was explicitly extracted and turned out to be identical to the corresponding equilibrium value to first order in the perturbation expansion. Further relevant studies were consistent with our conclusion; we also provided an argument that this result may persist to all orders in the perturbation series.

We then numerically solved the complex Ginzburg-Landau equation on a two-dimensional square lattice using a finite-differential method. Intriguing patterns emerge in this regime, where topological defects play a very important role since they can emit spiral waves. We reported non-universal dynamical and aging scaling behavior in both the focusing and defocusing spiral case after system was quenched close to the real Ginzburg-Landau equation limit. Related non-universal aging and auto-correlation exponents were numerically calculated.

Finally, we also investigated the transition from the strongly chaotic “defect turbulence” state to a frozen state when the control parameter pair is quenched beyond the limit of stability for the defect chaos state, which hence becomes metastable. The establishment of stable spiral structures is induced by nucleation processes. A finite dimensionless barrier was extracted for the deep-quench case in the infinite system size limit, which suggests that the associated transition is discontinuous. A detailed analysis of the nucleation time distribution for the near-transition limit case revealed an exponential decay behavior in the long tails of these distributions. This is consistent with a discontinuous transition scenario as well. We also studied the nucleation of another interesting pattern, namely target wave structures, which emerge if spatial inhomogeneities are introduced. Similar results and conclusions as the near-crossover limit case of spiral wave nucleation apply in this situation.

We hope these comprehensive studies of non-equilibrium dynamical phenomena described by complex Ginzburg-Landau equation using both analytical and numerical approaches will further aid researchers to more comprehensively understand the complex behavior of nonlinear dynamical systems.

Bibliography

[1] H. Hinrichsen, Physica A: Statistical Mechanics and its Applications **369**, 1 (2006).

[2] U. C. Täuber, Annual Review of Condensed Matter Physics **8**, 185 (2017).

[3] L. Sieberer, S. Huber, E. Altman, and S. Diehl, Physical Review Letters **110**, 195301 (2013).

[4] L. Sieberer, S. Huber, E. Altman, and S. Diehl, Physical Review B **89**, 134310 (2014).

[5] U. C. Täuber and S. Diehl, Physical Review X **4**, 021010 (2014).

[6] U. C. Täuber, *Critical dynamics: a field theory approach to equilibrium and non-equilibrium scaling behavior* (Cambridge: Cambridge University Press, 2014).

[7] I. S. Aranson and L. Kramer, Reviews of Modern Physics **74**, 99 (2002).

[8] P. Manneville and H. Chaté, Physica D: Nonlinear Phenomena **96**, 30 (1996).

[9] H. Sakaguchi, Progress of Theoretical Physics **84**, 792 (1990).

[10] P. S. Hagan, SIAM Journal on Applied Mathematics **42**, 762 (1982).

[11] T. Bohr, G. Huber, and E. Ott, Physica D: Nonlinear Phenomena **106**, 95 (1997).

[12] H. Janssen, B. Schaub, and B. Schmittmann, Zeitschrift für Physik B Condensed Matter **73**, 539 (1989).

[13] P. C. Hohenberg and B. I. Halperin, Reviews of Modern Physics **49**, 435 (1977).

[14] L. C. E. Struik, *Physical aging in amorphous polymers and other materials* (Citeseer, 1977).

[15] C. A. Angell, Science **267**, 1924 (1995).

[16] M. Henkel and M. Pleimling, *Non-Equilibrium Phase Transitions: Volume 2: Ageing and Dynamical Scaling Far from Equilibrium* (Dordrecht: Springer, 2010).

[17] R. Becker and W. Döring, Annalen der Physik **416**, 719 (1935).

[18] D. Turnbull and J. C. Fisher, The Journal of Chemical Physics **17**, 71 (1949).

[19] D. W. Oxtoby, Journal of Physics: Condensed Matter **4**, 7627 (1992).

[20] D. W. Oxtoby, Accounts of Chemical Research **31**, 91 (1998).

[21] J. M. Garcıa-Ruiz, Journal of Structural Biology **142**, 22 (2003).

[22] R. P. Sear, Journal of Physics: Condensed Matter **19**, 033101 (2007).

[23] W. Liu and U. C. Täuber, Journal of Physics A: Mathematical and Theoretical **49**, 434001 (2016).

[24] D. J. Amit, *Field Theory, The Renormalization Group and Critical Phenomena* (Singapore: World Scientific, 1984).

[25] C. Itzykson and J.-M. Drouffe, *Statistical Field Theory: vols 1, 2* (Cambridge Univ. Press, 1989).

[26] H. Kleinert and V. Schulte-Frohlinde, *Critical Properties of* ϕ^4 *Theories* (Singapore: World Scientific, 2001).

[27] J. Zinn-Justin, *Quantum Field Theory and Critical Phenomena* (Clarendon Press, 2002).

[28] A. Vasiliev, *The field theoretic renormalization group in critical behavior theory and stochastic dynamics* (Chapman and Hall/CRC, 2004).

[29] R. Folk and G. Moser, Journal of Physics A: Mathematical and General **39**, R207 (2006).

[30] A. Kamenev, *Field theory of non-equilibrium systems* (Cambridge: Cambridge University Press, 2011).

[31] I. Carusotto and C. Ciuti, Reviews of Modern Physics **85**, 299 (2013).

[32] K. Baumann, C. Guerlin, F. Brennecke, and T. Esslinger, Nature **464**, 1301 (2010).

[33] H. Ritsch, P. Domokos, F. Brennecke, and T. Esslinger, Reviews of Modern Physics **85**, 553 (2013).

[34] F. Brennecke, R. Mottl, K. Baumann, R. Landig, T. Donner, and T. Esslinger, Proceedings of the National Academy of Sciences **110**, 11763 (2013).

[35] J. Clarke and F. K. Wilhelm, Nature **453**, 1031 (2008).

[36] M. J. Hartmann, F. G. Brandao, and M. B. Plenio, Laser & Photonics Reviews **2**, 527 (2008).

[37] A. A. Houck, H. E. Türeci, and J. Koch, Nature Physics **8**, 292 (2012).

[38] S. Schmidt and J. Koch, Annalen der Physik **525**, 395 (2013).

[39] F. Marquardt and S. M. Girvin, Physics **2**, 40 (2009).

[40] D. Chang, A. H. Safavi-Naeini, M. Hafezi, and O. Painter, New Journal of Physics **13**, 023003 (2011).

[41] M. Ludwig and F. Marquardt, Physical Review Letters **111**, 073603 (2013).

[42] A. Imamoglu, R. Ram, S. Pau, Y. Yamamoto, *et al.*, Physical Review A **53**, 4250 (1996).

[43] J. Kasprzak, M. Richard, S. Kundermann, A. Baas, P. Jeambrun, J. Keeling, F. Marchetti, M. Szymańska, R. André, J. Staehli, *et al.*, Nature **443**, 409 (2006).

[44] K. G. Lagoudakis, M. Wouters, M. Richard, A. Baas, I. Carusotto, R. André, L. S. Dang, and B. Deveaud-Plédran, Nature Physics **4**, 706 (2008).

[45] G. Roumpos, M. Lohse, W. H. Nitsche, J. Keeling, M. H. Szymańska, P. B. Littlewood, A. Löffler, S. Höfling, L. Worschech, A. Forchel, *et al.*, Proceedings of the National Academy of Sciences **109**, 6467 (2012).

[46] S. A. Moskalenko, S. A. Moskalenko, and D. Snoke, *Bose-Einstein condensation of excitons and biexcitons: and coherent nonlinear optics with excitons* (Cambridge: Cambridge University Press, 2000).

[47] J. Keeling, M. H. Szymanska, and P. B. Littlewood, *Optical Generation and Control of Quantum Coherence in Semiconductor Nanostructures* (Berlin: Springer, 2010).

[48] U. C. Täuber, V. K. Akkineni, and J. E. Santos, Physical Review Letters **88**, 045702 (2002).

[49] S. Utsunomiya, L. Tian, G. Roumpos, C. Lai, N. Kumada, T. Fujisawa, M. Kuwata-Gonokami, A. Löffler, S. Höfling, A. Forchel, *et al.*, Nature Physics **4**, 700 (2008).

[50] M. C. Cross and P. C. Hohenberg, Reviews of Modern Physics **65**, 851 (1993).

[51] M. Cross and H. Greenside, *Pattern formation and dynamics in nonequilibrium systems* (Cambridge: Cambridge University Press, 2009).

[52] E. Frey, Physica A: Statistical Mechanics and its Applications **389**, 4265 (2010).

[53] T. Risler, J. Prost, and F. Jülicher, Physical Review E **72**, 016130 (2005).

[54] E. Altman, L. M. Sieberer, L. Chen, S. Diehl, and J. Toner, Physical Review X **5**, 011017 (2015).

[55] P. Calabrese and A. Gambassi, Journal of Physics A: Mathematical and General **38**, R133 (2005).

[56] A. Chiocchetta, A. Gambassi, S. Diehl, and J. Marino, Physical Review B **94**, 174301 (2016).

[57] K. Oerding and H. Janssen, Journal of Physics A: Mathematical and General **26**, 3369 (1993).

[58] K. Oerding and H. Janssen, Journal of Physics A: Mathematical and General **26**, 5295 (1993).

[59] B. Zheng, International Journal of Modern Physics B **12**, 1419 (1998).

[60] M. Krech, Physical Review E **55**, 668 (1997).

[61] G. L. Daquila and U. C. Täuber, Physical Review E **83**, 051107 (2011).

[62] M. Henkel, J. D. Noh, and M. Pleimling, Physical Review E **85**, 030102 (2012).

[63] G. L. Daquila and U. C. Täuber, Physical Review Letters **108**, 110602 (2012).

[64] J. J. Ramasco, M. Henkel, M. A. Santos, and C. A. da Silva Santos, Journal of Physics A: Mathematical and General **37**, 10497 (2004).

[65] S. Chen and U. C. Täuber, Physical Biology **13**, 025005 (2016).

[66] H.-K. Janssen, Zeitschrift für Physik B Condensed Matter **23**, 377 (1976).

[67] C. D. Dominicis, in *J. Phys.(Paris), Colloq* (1976) pp. C1–247.

[68] R. Bausch, H.-K. Janssen, and H. Wagner, Zeitschrift für Physik B Condensed Matter **24**, 113 (1976).

[69] H. W. Diehl, *Phase Transitions and Critical Phenomena* (Academic, London, 1986).

[70] M. Henkel and X. Durang, Journal of Statistical Mechanics: Theory and Experiment **2015**, P05022 (2015).

[71] M. Wouters and I. Carusotto, Physical Review Letters **105**, 020602 (2010).

[72] M. Wouters, T. Liew, and V. Savona, Physical Review B **82**, 245315 (2010).

[73] C. Gardiner and P. Zoller, *Quantum noise: a handbook of Markovian and non-Markovian quantum stochastic methods with applications to quantum optics*, Vol. 56 (Springer Science & Business Media, 2004).

[74] M. Henkel, M. Pleimling, C. Godreche, and J. M. Luck, Physical Review Letters **87**, 265701 (2001).

[75] M. Pleimling, Physical Review B **70**, 104401 (2004).

[76] B. L. Brown, U. C. Täuber, and M. Pleimling, Physical Review B **97**, 020405 (2018).

[77] P. Coullet, L. Gil, and J. Lega, Physical Review Letters **62**, 1619 (1989).

[78] G. Huber, P. Alstrøm, and T. Bohr, Physical Review Letters **69**, 2380 (1992).

[79] S. K. Das, Europhysics Letters **97**, 46006 (2012).

[80] H. Chaté and P. Manneville, Physica A: Statistical Mechanics and its Applications **224**, 348 (1996).

[81] S. Abriet and D. Karevski, The European Physical Journal B **37**, 47 (2004).

[82] S. Puri, S. K. Das, and M. Cross, Physical Review E **64**, 056140 (2001).

[83] A. Zaikin and A. Zhabotinsky, Nature **225**, 535 (1970).

[84] A. T. Winfree, Science **175**, 634 (1972).

[85] A. T. Winfree, Science **181**, 937 (1973).

[86] S. C. Müller, T. Plesser, and B. Hess, Physica D: Nonlinear Phenomena **24**, 87 (1987).

[87] G. S. Skinner and H. L. Swinney, Physica D: Nonlinear Phenomena **48**, 1 (1991).

[88] T. Reichenbach, M. Mobilia, and E. Frey, Physical Review E **74**, 051907 (2006).

[89] T. Reichenbach, M. Mobilia, and E. Frey, Nature **448**, 1046 (2007).

[90] Q. He, M. Mobilia, and U. C. Täuber, The European Physical Journal B **82**, 97 (2011).

[91] S. R. Serrao and U. C. Täuber, Journal of Physics A: Mathematical and Theoretical **50**, 404005 (2017).

[92] F. Daviaud, J. Lega, P. Bergé, P. Coullet, and M. Dubois, Physica D: Nonlinear Phenomena **55**, 287 (1992).

[93] Q. Feng, W. Pesch, and L. Kramer, Physical Review A **45**, 7242 (1992).

[94] I. Rehberg, S. Rasenat, and V. Steinberg, Physical Review Letters **62**, 756 (1989).

[95] P. Coullet and J. Lega, Europhysics Letters **7**, 511 (1988).

[96] S. Komineas, F. Heilmann, and L. Kramer, Physical Review E **63**, 011103 (2000).

[97] I. Aranson, H. Levine, and L. Tsimring, Physical Review Letters **72**, 2561 (1994).

[98] H. Zhang, B. Hu, G. Hu, Q. Ouyang, and J. Kurths, Physical Review E **66**, 046303 (2002).

[99] C. Zhang, H. Zhang, Q. Ouyang, B. Hu, and G. H. Gunaratne, Physical Review E **68**, 036202 (2003).

[100] K. Nam, E. Ott, M. Gabbay, and P. N. Guzdar, Physica D: Nonlinear Phenomena **118**, 69 (1998).

[101] P. S. Hagan, Advances in Applied Mathematics **2**, 400 (1981).

[102] N. Kopell, Advances in Applied Mathematics **2**, 389 (1981).

[103] N. Kopell and L. Howard, Advances in Applied Mathematics **2**, 417 (1981).

[104] A. E. Bugrim, M. Dolnik, A. M. Zhabotinsky, and I. R. Epstein, The Journal of Physical Chemistry **100**, 19017 (1996).

[105] M. Hendrey, K. Nam, P. Guzdar, and E. Ott, Physical Review E **62**, 7627 (2000).

[106] M. Jiang, X. Wang, Q. Ouyang, and H. Zhang, Physical Review E **69**, 056202 (2004).

[107] A. C. Newell and J. A. Whitehead, Journal of Fluid Mechanics **38**, 279 (1969).

[108] Y. Kuramoto, *Chemical oscillations, waves, and turbulence* (Courier Corporation, 2003).

[109] A. Newell, Annual Review of Fluid Mechanics **25**, 399 (1993).

[110] I. Aranson, L. Aranson, L. Kramer, and A. Weber, Physical Review A **46**, R2992 (1992).

[111] A. Weber, L. Kramer, I. Aranson, and L. Aranson, Physica D: Nonlinear Phenomena **61**, 279 (1992).

[112] L. Kramer and W. Zimmermann, Physica D: Nonlinear Phenomena **16**, 221 (1985).

[113] L. S. Tuckerman and D. Barkley, Physica D: Nonlinear Phenomena **46**, 57 (1990).

[114] B. Janiaud, Physica D: Nonlinear Phenomena **55**, 269 (1992).

[115] L. D. Landau and E. Lifshitz, *Course of Theoretical Physics Vol. 6 Fluid Mechanies* (Pergamon Press, 1959).

[116] J. T. Stuart and R. Di Prima, Proceedings of the Royal Society of London. A. Mathematical and Physical Sciences **372**, 357 (1980).

[117] P. Coullet, L. Gil, and J. Lega, Physica D: Nonlinear Phenomena **37**, 91 (1989).

[118] B. I. Shraiman, A. Pumir, W. van Saarloos, P. C. Hohenberg, H. Chaté, and M. Holen, Physica D: Nonlinear Phenomena **57**, 241 (1992).

[119] T. Bohr, A. W. Pedersen, and M. H. Jensen, Physical Review A **42**, 3626 (1990).

[120] P. S. Hagan, SIAM Journal on Applied Mathematics **42**, 762 (1982).

[121] A. V. Gaponov-Grekhov and M. I. Rabinovich, Physics-Uspekhi **30**, 433 (1987).

[122] L. Gil, J. Lega, and J. Meunier, Physical Review A **41**, 1138 (1990).

[123] J. Lega, Computer Methods in Applied Mechanics and Engineering **89**, 419 (1991).

[124] H. Wang, Physical Review Letters **93**, 154101 (2004).

[125] D. Bishop and J. Reppy, Physical Review B **22**, 5171 (1980).

[126] J. M. Davidenko, P. Kent, and J. Jalife, Physica D: Nonlinear Phenomena **49**, 182 (1991).

[127] M. Hendrey, E. Ott, and T. M. Antonsen Jr, Physical Review E **61**, 4943 (2000).

[128] V. M. Eguiluz, E. Hernández-García, and O. Piro, International Journal of Bifurcation and Chaos **9**, 2209 (1999).

[129] T. Bohr, G. Huber, and E. Ott, Europhysics Letters **33**, 589 (1996).

[130] R. Braun and F. Feudel, Physical Review E **53**, 6562 (1996).

[131] S. K. Das, Physical Review E **87**, 012135 (2013).

[132] S. Patra and S. K. Das, The European Physical Journal E **36**, 130 (2013).

[133] I. S. Aranson, L. Kramer, and A. Weber, Physical Review E **47**, 3231 (1993).

[134] I. S. Aranson, L. Kramer, and A. Weber, Physical Review E **48**, R9 (1993).

[135] H. Sakaguchi, Progress of Theoretical Physics **82**, 7 (1989).

[136] I. S. Aranson, H. Chaté, and L.-H. Tang, Physical Review Letters **80**, 2646 (1998).

[137] Several simulation movies for different parameter regimes and scenarios are available at this URL: `http://www1.phys.vt.edu/~tauber/CGLEMovies/` (2019), (Generated by W. Liu).

[138] G. F. Mazenko, Physical Review E **64**, 016110 (2001).

[139] E. J. Neves and R. H. Schonmann, Communications in Mathematical Physics **137**, 209 (1991).

[140] K. Park, P. A. Rikvold, G. M. Buendía, and M. Novotny, Physical Review Letters **92**, 015701 (2004).

[141] V. K. Vanag and I. R. Epstein, Science **294**, 835 (2001).

[142] B. Li, X. Gao, Z. Deng, H. Ying, and H. Zhang, Europhysics Letters **91**, 34001 (2010).